A dynamic bactofilin cytoskeleton recruits an M23 endopeptidase to control bacterial morphogenesis

Manuel Osorio-Valeriano[1,2,#,*], Emöke Cserti[1,*], Sebastian Pöhl[1], Rogelio Hernández-Tamayo[3,4], Jacob Biboy[5], Patrick Sobetzko[4,§], Waldemar Vollmer[5], Peter L. Graumann[3,4], Martin Thanbichler[1,2,4]

[1] Department of Biology, University of Marburg, Marburg, Germany
[2] Max Planck Institute for Terrestrial Microbiology, Marburg, Germany
[3] Department of Chemistry, University of Marburg, Marburg, Germany
[4] Center for Synthetic Microbiology (SYNMIKRO), Marburg, Germany
[5] Centre for Bacterial Cell Biology, Institute for Cell and Molecular Biosciences, Newcastle University, Newcastle upon Tyne, United Kingdom

[#] Present address: Department of Cell Biology, Blavatnik Institute, Harvard Medical School, Boston, MA, USA.
[§] Present address: Faculty of Sciences and Technologies, Université de Lorraine, Nancy, France.

* These authors contributed equally to this work.

Address correspondence to
Martin Thanbichler (thanbichler@uni-marburg.de)

Keywords
Cell wall, peptidoglycan, cell shape, autolysin, LytM domain, bacterial cell division, divisome, elongasome

Abstract

Bactofilins have emerged as a widespread family of cytoskeletal proteins with important roles in bacterial morphogenesis, but their precise mode of action is still incompletely understood. Here, we identify the bactofilin cytoskeleton as a key regulator of cell growth in the stalked budding alphaproteobacterium *Hyphomonas neptunium*. We show that in this species, the lack of bactofilins causes severe morphological defects, resulting from unconstrained growth of the stalk and bud compartments. In line with this finding, bactofilin polymers localize dynamically to the stalk base and then to the incipient bud neck prior to the onset of bud formation, suggesting that they act as a barrier that retains the cell wall biosynthetic machinery in the respective growth zones. Notably, in a broad range of species, bactofilin genes lie adjacent to genes encoding cell wall hydrolases of the M23 peptidase family. We show that the corresponding *H. neptunium* endopeptidase, LmdC, is a bitopic membrane protein with peptidoglycan hydrolase activity that colocalizes with the bactofilin cytoskeleton, dependent on a direct interaction of its cytoplasmic tail with the bactofilin cytoskeleton. A functional association of bactofilins with M23 peptidases is further verified by studies of the spiral-shaped alphaproteobacterium *Rhodospirillum rubrum*, whose bactofilin and LmdC homologs colocalize at the inner cell curvature, forming a complex that modulates the degree of cell helicity. These findings indicate that bactofilins and M23 peptidases form a conserved functional module that is critical for cell shape determination in morphologically complex bacteria.

Introduction

17 Bacteria come in a variety of different cell shapes, which can be further modified by the formation of
18 cellular extensions such as branches or stalks (Kysela et al., 2016; Yang et al., 2016). Their morphology can
19 change as a function of the cell cycle or in response to environmental cues to ensure optimal fitness in
20 the given ecological niche or growth conditions (van Teeseling et al., 2017; Yang et al., 2016). In the vast
21 majority of species, cell shape is determined by the peptidoglycan cell wall, a complex macromolecule
22 composed of glycan chains that are crosslinked by short peptides (Typas et al., 2012; Vollmer et al., 2008).
23 The synthesis of this mesh-like structure is achieved by an array of synthetic and lytic enzymes that are
24 typically combined into multi-protein complexes and associated with regulatory factors and cytoskeletal
25 elements to facilitate the coordination and spatiotemporal regulation of their activities (Egan et al., 2020;
26 Rohs and Bernhardt, 2021).

27 Basic spherical, rod-like and hyphal shapes are generated by the combined action of the cell division and
28 cell elongation machinery (Margolin, 2009; Rohs and Bernhardt, 2021). In most bacteria, cell division is
29 executed by the divisome, which is organized by the tubulin homolog FtsZ and mediates cell constriction
30 and the synthesis of the new cell poles prior to cytokinesis (McQuillen and Xiao, 2020). Cell elongation, by
31 contrast, can be achieved by various types of cell wall-biosynthetic complexes, including the so-called
32 elongasome, which is organized by the actin homolog MreB and mediates the dispersed incorporation of
33 new cell wall material along the lateral cell walls (Shi et al., 2018), or different cell pole-associated com-
34 plexes that promote polar growth of the cell body (Brown et al., 2011). More complex cell shapes are
35 generated with the help of accessory systems that either modulate the activity of the generic cell elon-
36 gation machinery or have peptidoglycan biosynthetic activity on their own, thereby locally modifying the
37 structure of the peptidoglycan layer (Taylor et al., 2019).

38 A particularly widespread family of cytoskeletal proteins implicated in cell shape modification are the
39 bactofilins. They are characterized by a conserved central Bactofilin A/B domain (InterPro ID: IPR007607;
40 Paysan-Lafosse et al., 2022) with a barrel-like β-helical fold that is typically flanked by short disordered
41 terminal regions (Kühn et al., 2010; Shi et al., 2015; Vasa et al., 2015). Bactofilins polymerize spontane-
42 ously without the need for nucleotide cofactors (Koch et al., 2011; Kühn et al., 2010), driven by head-to-
43 head and tail-to-tail interactions between the core domains of neighboring molecules (Deng et al., 2019).
44 Lateral interactions between individual protofilaments can then give rise to higher-order assemblies, such
45 as bundles or two-dimensional sheets (Kühn et al., 2010; Vasa et al., 2015; Zuckerman et al., 2015).
46 Previous work has suggested that bactofilin polymers typically associate with the inner face of the cyto-

47 plasmic membrane and localize to regions of high membrane curvature (Caccamo et al., 2020; Hay et al.,
48 1999; Kühn et al., 2010; Lin et al., 2017; Taylor et al., 2020). These structures have been co-opted as
49 localization determinants and assembly platforms by several different morphogenetic systems.

50 For instance, bactofilin homologs were reported to contribute to rod-shape maintenance in *Myxococcus*
51 *xanthus* (Koch et al., 2011), the establishment of helical cell shape in the human pathogen *Helicobacter*
52 *pylori* (Sycuro et al., 2010; Taylor et al., 2020) as well as the modulation of cell helicity in the spiral-shaped
53 bacterium *Leptospira biflexa* (Jackson et al., 2018). Apart from modulating general cell shape, they were
54 found to have an important role in the formation of cellular extensions known as stalks, which are wide-
55 spread among alphaproteobacterial species (Wagner and Brun, 2007). Stalks are elongated protrusions of
56 the cell envelope that are filled with a thin thread of cytoplasm and grow through zonal incorporation of
57 cell wall material at their base (Aaron et al., 2007; Randich and Brun, 2015). In *Caulobacter crescentus* and
58 *Asticcacaulis biprosthecum*, bactofilin polymers were shown to localize to the stalk base to direct proper
59 stalk formation. In *C. crescentus*, they recruit a cell wall synthase that contributes to stalk elongation, with
60 their absence leading to a reduction in stalk length (Kühn et al., 2010). In *A. biprosthecum*, by contrast,
61 bactofilin acts as a central topological regulator that is required to efficiently initiate stalk formation and
62 limit peptidoglycan biosynthesis to the stalk base. Its absence leads to the development of pseudostalks,
63 which are much shorter and wider than normal stalks and irregularly shaped, likely due to unrestrained
64 peptidoglycan biosynthesis through the entire stalk envelope (Caccamo et al., 2020).

65 While stalks are often accessory structures with highly specialized functions (Klein et al., 2013; Persat et
66 al., 2014; Wagner and Brun, 2007), stalked budding bacteria such as *Hyphomonas neptunium* and other
67 members of the *Hyphomonadaceae* and *Hyphomicrobiaceae* use them as integral parts of the cell with
68 key roles in cell growth and division (Moore, 1981). *H. neptunium* has a biphasic life cycle (Wali et al.,
69 1980), in which a non-replicative, motile swimmer cell sheds its single polar flagellum and differentiates
70 into a replicative, sessile stalked cell (**Figure 1—figure supplement 1**). Unlike most widely studied model
71 species, it does not divide by binary fission but instead produces new offspring through the formation of
72 buds at the tip of the stalk. As the terminal stalk segment gradually dilates, a flagellum is formed at the
73 pole opposite the stalk. After DNA replication and translocation of one of the sister chromosomes through
74 the stalk into the bud compartment (Jung et al., 2019), cytokinesis occurs at the bud neck, releasing a new
75 swimmer cell. While the newborn cell first needs to differentiate into stalked cells to start replication, the
76 stalked mother cell restores the stalk and then immediately re-enters the next budding cycle (Jung et al.,
77 2019; Wali et al., 1980). The developmental program of *H. neptunium* involves several switches in the

78 pattern of peptidoglycan biosynthesis (Cserti et al., 2017). After birth, swimmer cells increase in size by
79 dispersed incorporation of new cell wall material throughout the cell body. Stalk formation is then
80 achieved by zonal growth at the stalk base, followed by localized dispersed growth of the stalk-terminal
81 bud compartment and, finally, zonal peptidoglycan synthesis at the site of cell division. The pattern of
82 new cell wall synthesis is similar to the localization pattern of elongasome components (Cserti et al., 2017),
83 suggesting the involvement of this machinery in all growth phases. However, the underlying regulatory
84 mechanisms are still unknown.

85 In this study, we identify the bactofilin cytoskeleton as a central player in the regulation of cell growth in
86 *H. neptunium*. We show that in this organism bactofilin polymers localize dynamically to the stalk base
87 and the bud neck, with their absence leading to unconstrained growth of the stalk and bud compartments,
88 indicating a central role in the spatial regulation of cell wall biosynthesis. Interestingly, database searches
89 reveal that in a range of different species bactofilin genes are clustered with genes for cell wall hydrolases
90 of the M23 peptidase family, suggesting a functional connection between these two types of proteins. We
91 find that the *H. neptunium* M23 peptidase homolog LmdC indeed consistently colocalizes with the bacto-
92 filin cytoskeleton *in vivo* and interacts directly with bactofilin *in vitro*. Studies in the spiral-shaped alpha-
93 proteobacterium *Rhodospirillum rubrum* again reveal a close association of its bactofilin and LmdC homo-
94 logs, which colocalize in regions of positive inner cell curvature and are both required to ensure proper
95 cell helicity. Collectively, these demonstrate a conserved functional interaction between bactofilins and
96 M23 peptidases that is important for the control of cell growth in morphologically complex bacteria.

Results

97 **The bactofilin cytoskeleton is required for cell shape determination in *H. neptunium***

98 The *H. neptunium* chromosome contains two open reading frames that encode bactofilin homologs,
99 HNE_0444 and HNE_2629 (Badger et al., 2006). Reciprocal BLAST analysis using the two bactofilins
100 described in the close relative *C. crescentus* identified HNE_2629 as a potential ortholog of *C. crescentus*
101 BacA (43% identity, 60% similarity). By contrast, HNE_0444 was only distantly related (<30% identity) to
102 either of the two proteins. Based on these results, we propose to designate the two bactofilin homologs
103 of *H. neptunium* BacA (HNE_2629) and BacD (HNE_0444), respectively. *bacA* forms a putative bicistronic
104 operon with *lmdC*, an essential gene encoding an M23 peptidase homolog (Cserti et al., 2017) (**Figure 1A**).
105 The two genes overlap by 17 base pairs, suggesting that their expression is closely coupled. *bacD*, by
106 contrast, is not part of an operon. Both BacA and BacD display the typical architecture of bactofilins, with
107 a central polymerization domain flanked by short non-structured N- and C-terminal regions (**Figure 1B**).

108 To investigate the role of bactofilins in *H. neptunium*, we generated mutant strains in which *bacA* and
109 *bacD* were deleted either individually or in combination. Upon light and electron microscopic analysis,
110 Δ*bacA* and Δ*bacAD* cells showed severe morphological defects, as reflected by irregularly shaped, elon-
111 gated and/or oversized cells, buds directly fused with the mother cell body, branched stalks, and multiple
112 wide protrusions that emerged from the cells in an apparently random fashion (**Figures 1C-F**), reminiscent
113 of the pseudostalks reported for a bactofilin-deficient *A. biprosthecum* mutant (Caccamo et al., 2020). The
114 wild-type phenotype could be largely restored by expressing an ectopic copy of *bacA* under the control of
115 a copper-inducible promoter, even though BacA accumulated to lower-than-normal levels under this
116 condition (**Figure 1—figure supplement 2A-C**), confirming the absence of polar effects. The deletion of
117 *bacD*, by contrast, did not cause any obvious cell shape defects (**Figures 1C,F** and **Figure 1—figure supple-**
118 **ment 2D**). Moreover, neither *bacD* deletion (**Figure 1C,F**) nor *bacD* overexpression (**Figure 1—figure**
119 **supplement 2C,E**) had any influence on the proportion of distorted or amorphous cells in the Δ*bacA*
120 background. These results demonstrate that BacA has a critical role in the regulation of cell growth in
121 *H. neptunium*, whereas BacD might be an auxiliary factor of so-far unknown function, similar to BacB in
122 *C. crescentus*.

123 To obtain more insight into the dynamics of cell growth in the Δ*bacA* mutant and identify the initial pheno-
124 typic defects induced upon BacA depletion, we imaged a conditional *bacA* mutant after its transfer from
125 permissive to restrictive conditions on an agarose pad (**Figure 2A,B**). Following cells at the swimmer-to-
126 stalked cell transition, we observed that stalk formation initially proceeded as in the wild-type strain.

127 However, as BacA was gradually depleted, stalk elongation ceased and the stalk structure started to widen
128 and eventually develop multiple bulges that kept on expanding in an apparently uncontrolled manner.
129 Thus, BacA appears to be required to maintain the polar growth zone at the stalk base, with its absence
130 leading to unconstrained growth of the stalk cell wall. To follow the fate of bactofilin-deficient cells over
131 a prolonged period of time, we monitored Δ*bacAD* cells in a flow-cell system, which ensured optimal
132 nutrient supply throughout the course of the experiment and led to a looser packing of cells, thereby
133 facilitating their visual analysis (**Figure 2—figure supplement 1** and **Video 1**). In this setup, cells again
134 started growth by the formation of irregularly shaped stalks that started to branch, with branches deve-
135 loping either into extensive hyphal-like structures or large, amorphous compartments that may represent
136 morphologically aberrant buds. At irregular intervals, cells divided at the junctions between hyphal and
137 bulged cellular segments, releasing smaller amorphous fragments and, occasionally, also cells with close-
138 to-normal morphology. Wild-type cells, by contrast, showed the usual growth pattern when cultivated
139 under these conditions (**Video 2**). Together, these results underscore the importance of BacA in the
140 spatiotemporal control of cell growth in *H. neptunium*.

141 To obtain more detailed information about the dynamics of cell wall biosynthesis in the absence of bacto-
142 filins, we performed pulse-labeling studies with the fluorescent D-amino acid HADA, which is rapidly incor-
143 porated into peptidoglycan when added to the culture medium, thus marking regions of ongoing cell wall
144 biosynthesis (Kuru et al., 2015). Wild-type cells showed the typical succession of growth modes, with
145 dispersed growth in swimmer cells, zonal growth at the stalk base in stalked cells and localized dispersed
146 growth in the nascent bud (**Figure 2C**). In the Δ*bacAD* background, by contrast, this switch in the growth
147 modes was abolished. Cells with close-to-normal morphology that had just initiated stalk formation still
148 showed a distinct fluorescent focus at the stalked pole, suggesting that the initial recruitment of the
149 machinery responsible for stalk formation occurred in a bactofilin-independent manner. However, all
150 other cell types, including amorphous cells with aberrant stalk- and bud-like extensions, only displayed
151 diffuse fluorescence, which points to uncontrolled growth through dispersed incorporation of new pepti-
152 doglycan throughout the entire cell envelope. These findings support the notion that the bactofilin cyto-
153 skeleton is required to limit cell wall biosynthesis to the different growth zones of *H. neptunium*.

154 **Bactofilins localize dynamically to the boundaries of the *H. neptunium* growth zones**

155 Despite their severe cell shape defects, the Δ*bacA* and Δ*bacAD* mutants showed only a moderate decrease
156 in their apparent growth rates (**Figure 2—figure supplement 2A**), and the global composition of their
157 peptidoglycan remained essentially unchanged (**Figure 2—figure supplement 2B** and **Dataset 1**). These

158 findings suggested that BacA might affect cell wall composition at a local scale or act mainly by modulating
159 the activity of the generic cell elongation machinery. To further investigate the role of bactofilins in *H. nep-*
160 *tunium*, we first aimed to verify the ability of the proteins to assemble into polymeric scaffolds. A model
161 of the structure of BacA generated with AlphaFold-Multimer (Evans et al., 2022) suggested that the
162 protein adopted a β-helical fold and polymerized through head-to-head and tail-to-tail interactions among
163 different subunits (**Figure 3A**), as revealed previously in experimental studies (Deng et al., 2019; Shi et al.,
164 2015). Consistent with this prediction, purified BacA produced a mixture of long filaments, filament
165 bundles and two-dimensional polymeric sheets *in vitro*, which could be readily visualized by transmission
166 electron microscopy (**Figure 3B**). Moreover, upon heterologous co-expression in *Escherichia coli*, fluores-
167 cently tagged derivatives of BacA and BacD colocalized into extended filamentous structures that were
168 associated with the cell envelope (**Figure 3C**). These results confirm the polymeric nature of bactofilin
169 assemblies in *H. neptunium* and suggest that BacA and BacD interact with each other *in vivo*.

170 Next, we sought to investigate the localization dynamics of the bactofilin cytoskeleton *in vivo*. To this end,
171 we generated strains producing fluorescently tagged BacA or BacD derivatives in place of the native pro-
172 teins (**Figure 4—figure supplement 1**). Time-lapse microscopy analysis of cells producing a BacA-YFP
173 fusion on agarose pads (**Figure 4A**) revealed that the protein was localized to the new cell pole in swimmer
174 cells and remained associated with the stalk base during the initial phase of stalk formation. At some
175 point, it appeared to attach to the stalk structure and then move away from the base as new cell wall
176 material was inserted. Subsequently, stalk elongation ceased and the terminal stalk segment, delimited
177 by the bactofilin assembly, started to swell and develop into a bud, gradually displacing BacA-YFP in the
178 direction of the stalk base as its size increased. After cell division, both the mother cell and the newborn
179 swimmer cells showed a fluorescent focus, indicating that the bactofilin assembly was split during cell
180 division. To monitor the dynamics of the bactofilin cytoskeleton over multiple division cycles, we analyzed
181 the same strain in a flow-cell system (**Figure 4—figure supplement 2** and **Videos 3-5**). Under these condi-
182 tions, the small, newborn swimmer cells were washed away immediately after cytokinesis, preventing the
183 formation of microcolonies around the mother cell. We observed that cell division occurred at a small
184 distance from the BacA-YFP focus, leaving a short stalk-terminal segment in between the bactofilin assem-
185 bly and the stalk tip. After cytokinesis, the stalk elongated again prior to the initiation of the next budding
186 event. Notably, BacA-YFP was only occasionally detected at the stalked pole during the stalk restoration
187 phase, suggesting that the bactofilin cytoskeleton no longer plays a major role in stalk growth once the
188 stalk structure has been established. To verify the behavior observed in the time-lapse studies, we per-
189 formed a population-wide analysis of the BacA-YFP localization pattern, based on snap-shot images of

190 exponentially growing cells. A demographic analysis confirmed that the protein localizes to the new cell
191 pole in swimmer cells, remains at the stalk base in cells with short stalks and then moves to a position
192 close to the distal end of the stalk before the onset of budding, remaining associated with the bud neck
193 up to the point of cell division (**Figure 4B**). A very similar behavior was observed for a BacD-Venus fusion
194 (**Figure 4C**), consistent with the notion that the two bactofilin paralogs interact. In support of this hypo-
195 thesis, studies of a strain in which both proteins were fluorescently labeled showed that BacA and BacD
196 indeed colocalized at all stages of the developmental cycle (**Figures 4D** and **Figure 4—figure supplement**
197 **3A**). In the absence of BacA, BacD-Venus still formed distinct foci, albeit at apparently random positions
198 within the cell (**Figure 4—figure supplement 3B**). Notably, a BacA-YFP variant carrying a previously
199 reported mutation that disrupts the polymerization interface (F130R) (Deng et al., 2019; Vasa et al., 2015;
200 Zuckerman et al., 2015) was evenly distributed within the cell and unable to functionally replace the wild-
201 type protein, indicating that the formation of polymeric assemblies is essential for proper BacA locali-
202 zation and function (**Figure 4—figure supplement 4**). Given the localization of the bactofilin assemblies to
203 the stalk and bud boundaries and the unconstrained growth of these cellular structures in bactofilin-
204 deficient strains, we hypothesize that the bactofilin cytoskeleton has a critical role in limiting the cell wall
205 biosynthetic machinery to the different growth zones of *H. neptunium*.

206 **The assembly state of BacA changes at different stages of *H. neptunium* development**

207 Since bactofilins form highly stable polymers *in vitro* (Kühn et al., 2010; Zuckerman et al., 2015), the
208 dynamic localization observed for BacA and BacD was unexpected. To further characterize the dynamics
209 of the bactofilin cytoskeleton in *H. neptunium*, we followed the movement of individual BacA-YFP mole-
210 cules in swimmer, stalked and budding cells. First, we used single-molecule tracking data to generate high-
211 resolution images of the bactofilin assemblies in each of the three cell types. The results confirmed the
212 cell cycle-dependent localization patterns observed by widefield fluorescence microscopy (**Figure 5A**). In
213 addition, they revealed clusters in medial regions of the stalk, which may represent transient polymers
214 formed during the reshuffling of bactofilin molecules between the stalk base and the (incipient) bud neck.
215 When calculating the average mean squared displacement of the tracked BacA-YFP molecules, we found
216 that their mobility decreased gradually from the swimmer over the stalked cell to the budding cell stage
217 (**Figure 5B**). For each cell type, the distribution of step sizes in the single-particle tracks suggests the exis-
218 tence of two distinct diffusion regimes, with a static (D= 0.02 ± 0.0004 $\mu m^2 s^{-1}$) and a mobile (D= 0.35 ±
219 0.004 $\mu m^2 s^{-1}$) population, likely representing the polymerized and freely diffusible states, respectively
220 (**Figures 5C** and **Figure 5—figure supplement 1**). In swimmer cells, the static fraction comprised only ~60%
221 of the molecules. Its proportion increased to ~70% in stalked cells and finally reached ~80% in budding

222 cells. The F130R variant, by contrast, showed less than 15% of static molecules, consistent with the notion
223 that it is impaired in polymerization but still able to assemble under certain conditions after undergoing a
224 structural change that generates an alternative polymerization interface (Deng et al., 2019). Collectively,
225 these results show that, in *H. neptunium*, the assembly state of the bactofilin cytoskeleton changes as
226 cells progress through their developmental cycle. Moreover, despite the inherent stability of bactofilin
227 polymers, all cell types display a sizeable fraction of mobile BacA-YFP molecules, which could potentially
228 reflect the dynamic reorganization of bactofilin assemblies during cell growth.

229 **Bactofilin genes are often clustered with genes encoding M23 peptidases**

230 After identifying a critical role of BacA in *H. neptunium* morphogenesis, we set out to gain further insight
231 into its mechanism of action. Notably, in several species in which bactofilins play a role in cell shape deter-
232 mination, the corresponding bactofilin genes are located adjacent to genes encoding a putative M23
233 peptidase homologous to LmdC (**Figure 6A**). To determine whether this gene arrangement was more
234 widely conserved, we performed a comprehensive bioinformatic analysis in which we searched all bac-
235 terial genome sequences available for putative bactofilin genes that were located immediately upstream
236 or downstream of open reading frames encoding proteins with a predicted M23 peptidase domain. This
237 analysis identified a total of 226 species from a wide variety of bacterial phyla (**Figure 6B** and **Dataset 2**),
238 suggesting a conserved functional association between bactofilins and M23 peptidases.

239 **The M23 peptidase LmdC of *H. neptunium* has peptidoglycan hydrolase activity**

240 To clarify whether LmdC was also required for proper growth in *H. neptunium*, we aimed to generate a
241 mutant strain lacking LmdC activity. However, all attempts to delete the *lmdC* gene or the entire putative
242 *lmdC-bacA* operon or to generate non-functional truncated *lmdC* alleles were unsuccessful, in line with a
243 previous report suggesting that *lmdC* is essential for viability (Cserti et al., 2017). It was also not possible
244 to generate a conditional *lmdC* mutant producing the gene under the control of a copper-inducible pro-
245 moter, suggesting that its expression level needs to be precisely regulated.

246 Given that LmdC apparently had a critical role in *H. neptunium* growth, we went on to investigate the
247 physiological role of this protein. LmdC is a predicted bitopic membrane protein with a short N-terminal
248 cytoplasmic region, a transmembrane helix, large periplasmic region composed of a predicted coiled-coil
249 domain, and a C-terminal M23 peptidase domain (**Figure 7A**). Members of the M23 peptidase family
250 usually have Zn^{+}-dependent hydrolase activity and cleave bonds within the peptide side chains of in the
251 peptidoglycan meshwork (Firczuk et al., 2005; Grabowska et al., 2015). However, there are also various
252 representatives that have lost their enzymatic activity because of mutations in residues required for metal

253 cofactor binding and have instead adopted regulatory roles in cell wall biosynthesis (Figueroa-Cuilan et
254 al., 2021; Goley et al., 2010; Gurnani Serrano et al., 2021; Möll et al., 2010; Poggio et al., 2010; Uehara et
255 al., 2010). An amino acid alignment showed that the M23 peptidase domain of LmdC features all residues
256 reported to be critical for Zn^{2+} binding, suggesting that it could act as a genuine peptidogylcan hydrolase
257 (**Figure 7B**). In a structural model of LmdC generated with AlphaFold2 (Jumper et al., 2021), the peri-
258 plasmic coiled-coil and M23 peptidase domains form an elongated, rigid unit with two flanking non-
259 structured regions that is flexibly linked to the transmembrane helix (**Figure 7C**). Notably, LmdC homologs
260 were shown to form a distinct clade among the M23 peptidases that is broadly conserved among species
261 but particularly enriched in alpha- and deltaproteobacteria (Figueroa-Cuilan et al., 2021).

262 To clarify whether LmdC was indeed catalytically active, we purified a C-terminal fragment of the protein
263 including the M23 peptidase domain and assayed its activity *in vitro*. Peptidoglycan from *H. neptunium*
264 shows only a low degree of cross-linkage and hardly any pentapeptides (Cserti et al., 2017). We therefore
265 used normally crosslinked, pentapeptide-enriched peptidoglycan from *E. coli* strain D456 (lacking PBPs 4,
266 5 and 6) (Edwards and Donachie, 1993) as a substrate to enable a comprehensive analysis of the cleavage
267 specificity of LmdC. Upon treatment with the protein, the proportion of dimeric muropeptide species
268 strongly decreased, regardless of the length of the crosslinked peptides and without the formation of
269 major additional monomer peaks (**Figure 7D**). The activity of LmdC was particularly high at a pH value of
270 5, but the physiological significance of this effect remains to be determined. Collectively, these results
271 demonstrate that LmdC is a DD-endopeptidase cleaving the bond between the meso-diaminopimelic acid
272 residue of one peptide and D-alanine at position 4 of the other peptide, thereby reducing the degree of
273 cross-linkage within the peptidogycan layer (**Figure 7E**).

274 **LmdC associates with the bactofilin cytoskeleton in *H. neptunium***

275 To further investigate whether the peptidoglycan hydrolase LmdC was functionally linked to bactofilins in
276 *H. neptunium*, we set out to conduct *in vivo* co-localization studies. All attempts to generate fluorescently
277 labeled variants of full-length LmdC failed, because the fluorescent protein tags were cleaved off after
278 synthesis of the fusion proteins. However, we reasoned that in case LmdC was associated with the cyto-
279 plasmic bactofilin cytoskeleton, its recruitment might be mediated by its N-terminal cytoplasmic region,
280 which is predicted to fold into a short α-helix followed by a conspicuous β-hairpin (**Figure 7C**). To colocalize
281 the two proteins, we therefore generated a truncated reporter construct comprising only the N-terminal
282 cytoplasmic part and the transmembrane helix of LmdC fused to the red fluorescent protein mCherry
283 (Shaner et al., 2004) (**Figure 8A**). When produced in a *bacA-yfp* background, the fusion protein ($LmdC^{N}$-

284 mCherry) formed tight foci that perfectly colocalized with BacA-YFP and showed the characteristic cell
285 cycle-dependent localization pattern observed for the bactofilin assemblies (**Figures 8B,C**). This result
286 suggests that the N-terminal region of LmdC indeed associates with the bactofilin cytoskeleton, most likely
287 through interaction with its key component BacA. To further validate this hypothesis, we analyzed the
288 interaction between LmdC and BacA *in vitro* by biolayer interferometry. To this end, a synthetic peptide
289 comprising the cytoplasmic region of LmdC (amino acids 1-38) was immobilized on a biosensor and probed
290 with increasing concentrations of purified BacA protein. The results showed that BacA interacts with the
291 LmdC peptide with an apparent equilibrium dissociation constant (K_D) of ~15 µM. By contrast, an unrelat-
292 ed peptide used as a negative control was not bound with appreciable affinity (**Figures 8D,E**). This result
293 confirms a direct interaction between BacA and LmdC and identifies the N-terminal cytoplasmic region of
294 LmdC as the interaction determinant for BacA association. Notably, however, $LmdC^N$-mCherry still formed
295 foci in bactofilin-deficient cells, albeit at apparently random positions, suggesting that the protein can
296 assemble into larger complexes independently of its interaction with BacA (**Figure 8—figure supplement**
297 **1**).

298 ***R. rubrum* BacA recruits LmdC to the inner cell curvature to modulate spiral cell shape**

299 Our bioinformatic analysis suggests that bactofilins and M23 peptidases may be functionally associated in
300 a large number of species. To further explore this possibility, we turned our efforts to the spiral-shaped
301 bacterium *Rhodospirillum rubrum*, which contains a putative *lmdC-bacA* operon similar to that in *H. nep-*
302 *tunium* (Munk et al., 2011) (**Figure 9A**). The *R. rubrum* BacA homolog Rru_A1867 ($BacA_{Rs}$) is 37% identical
303 (57% similar) to BacA of *H. neptunium* and also consists of a central Bactofilin A/B domain flanked by
304 terminal non-structured regions (**Figure 9B**). The LmdC homolog Rru_A1868 ($LmdC_{Rs}$) is 39% identical
305 (55% similar) to *H. neptunium* LmdC and has a similar predicted molecular structure (Varadi et al., 2022).
306 The deletion of $bacA_{Rs}$ led to a noticeable increase in cell curvature (**Figures 9C** and **Figure 9—figure**
307 **supplement 1A**), as also reflected in a significant increase in cell sinuosity (**Figure 9D**). A very similar effect
308 was observed for cells lacking $lmdC_{Rs}$ or both $bacA_{Rs}$ and $lmdC_{Rs}$, indicating that the two gene products act
309 in the same pathway and jointly contribute to cell shape maintenance in *R. rubrum* (**Figures 9C,D and**
310 **Figure 1—figure supplement 1A**). In the two mutant strains, the global composition of peptidoglycan was
311 largely unchanged, supporting the notion that the $BacA_{Rs}$-$LmdC_{Rs}$ pathway modifies the cell wall only local-
312 ly or acts by modulating the activity of the generic cell elongation machinery (**Figure 9—figure supplement**
313 **1B**).

314 Complementation studies showed that the expression of a plasmid-borne *bacA* copy under the control of
315 a weak constitutive promoter attenuated the curvature defect, albeit only partially, likely due to inade-
316 quate expression levels (**Figure 9—figure supplement 2**). The generation of an analogous plasmid to
317 complement the deletion of $lmdC_{Rs}$ failed, because it was not possible to introduce the construct into
318 *Escherichia coli* for plasmid propagation, suggesting that the expression of $lmdC_{Rs}$ was toxic to the cells.
319 To further test this hypothesis, we constructed a plasmid enabling the inducible expression of the gene in
320 *E. coli*. Upon induction, a large part of the cell population lyzed, whereas control cells carrying an empty
321 plasmid did not show any phenotypic defects (**Figure 9—figure supplement 3**). These results indicate that,
322 similar to its *H. neptunium* homolog, $LmdC_{Rs}$ is an active enzyme with peptidoglycan hydrolase activity.

323 To determine how $BacA_{Rs}$ and $LmdC_{Rs}$ jointly affect cell curvature, we first generated an *R. rubrum* strain
324 that lacked $lmdC_{Rs}$ and carried a fully functional $bacA_{Rs}$-*mCherry* fusion (**Figure 9—figure supplement 2**)
325 in place of the native $bacA_{Rs}$ gene. Subsequently, we introduced a replicating plasmid that harbored a
326 constitutively expressed reporter construct encoding the predicted N-terminal cytoplasmic region and the
327 transmembrane helix (amino acids 1-80) of $LmdC_{Rs}$ fused to the green fluorescent protein mNeonGreen
328 (Shaner et al., 2013) ($LmdC^{N}_{Rs}$-mNG) (**Figure 9—figure supplement 4A,B**). We found that the two proteins
329 colocalized, forming patchy or filamentous structures that were preferentially, but not exclusively,
330 positioned at the inner cell curvature (**Figure 9E**). A very similar pattern was observed in the presence of
331 the wild-type $lmdC_{Rs}$ gene (**Figure 9—figure supplement 4C**). Importantly, the localization pattern of
332 $BacA_{Rs}$ was not affected by the absence of $LmdC_{Rs}$ (**Figure 9F**), whereas the $LmdC^{N}_{Rs}$-mNG fusion was com-
333 pletely dispersed in cells lacking $BacA_{Rs}$, indicating that $BacA_{Rs}$ acts as a localization determinant for $LmdC_{Rs}$
334 (**Figure 9G**). Collectively, these findings confirm a functional association between the bactofilin cyto-
335 skeleton and $LmdC_{Rs}$ in *R. rubrum*. Moreover, they lend support to the idea that bactofilins and M23 pepti-
336 dases form a conserved module involved in bacterial cell shape determination.

Discussion

337 Although bactofilins are widely conserved among bacteria, their cellular functions are still incompletely
338 understood. Here, we show that BacA homologs critically contribute to cell shape determination in two
339 morphologically distinct members of the alphaproteobacteria, the stalked budding bacterium *H. neptu-*
340 *nium* and the spiral-shaped bacterium *R. rubrum*. In both cases, they functionally interact with LmdC-type
341 DD-endopeptidases to promote local changes in the pattern of peptidoglycan biosynthesis. Bactofilins
342 thus complement the activities of the MreB and FtsZ cytoskeletons in the regulation of cell growth and
343 act as versatile cell shape modifiers that facilitate the establishment of complex bacterial morphologies.

344 In *H. neptunium*, the bactofilin cytoskeleton localizes dynamically to the stalk base and the bud neck, pro-
345 moting stalk growth and subsequent bud formation (**Figure 4**). While flanked by zones of active growth,
346 the stalk itself is usually devoid of cell wall biosynthetic machinery (Cserti et al., 2017). In bactofilin-
347 deficient cells, however, newly formed stalks are remodeled into wide and often branched cellular exten-
348 sions that grow in an apparently uncontrolled manner (**Figure 2** and **Figure 2—figure supplement 1**). This
349 observation suggests that bactofilin polymers establish barriers that normally prevent the entry of elonga-
350 some complexes from the mother cell or nascent bud compartments into the stalk. In their absence, the
351 stalk and bud growth zones are no longer confined and expand into the stalk envelope, leading to stalk
352 widening and the formation of irregular bulges due to uncontrolled peptidoglycan incorporation and bud
353 expansion. Bulges or larger amorphous segments at some point separate from the mother cell and then
354 continue to grow as independent cells, indicating that chromosome replication and segregation as well as
355 cell division still occur under these conditions.

356 The precise mechanism underlying the function of bactofilin in cell morphogenesis remains to be clarified.
357 It is conceivable that bactofilin polymers act by tethering peptidoglycan biosynthetic proteins or estab-
358 lishing physical barriers that hinder the mobility of elongasome complexes (**Figure 10A**). However, we
359 observed a close functional association of bactofilins with M23 peptidases that appears to be widely con-
360 served among species, suggesting that their activity may be intimately tied to cell wall hydrolysis. The
361 transition zones between the stalk and the adjacent mother cell and bud compartments are characterized
362 by a high degree of positive cell envelope curvature, which is in stark contrast to the negative curvature
363 in the remaining parts of the cell. The hydrolytic activity of *H. neptunium* LmdC may be critical to remodel
364 the cell wall in these zones. Importantly, MreB is thought to move along regions of negative inner curva-
365 ture (Hussain et al., 2018; Wong et al., 2019). The positively curved transition zones generated by the
366 bactofilin-LmdC assemblies could therefore represent topological barriers that are difficult to cross by

367 elongasome complexes, thereby helping to restrict their movement to the mother cell and bud compart-
368 ments. This effect may also be important during the stalk elongation phases following cell division, when
369 bactofilin assemblies are no longer present at the stalk base.

370 Notably, a role in stalk formation has also been reported for the bactofilin homologs of *C. crescentus* and
371 *A. biprosthecum*. In *C. crescentus*, the major bactofilin BacA was shown to act as a localization determinant
372 for the bifunctional penicillin-binding protein PbpC, a cell wall synthase that contributes to stalk elonga-
373 tion (Kühn et al., 2010) and the proper sorting of a stalk-specific protein (Hughes et al., 2013). However,
374 the absence of BacA only leads to a moderate reduction in stalk length and leaves overall cell shape
375 unaffected, indicating that this protein has only a minor role in *C. crescentus* stalk formation. In *A. bipros-*
376 *thecum*, by contrast, the deletion of *bacA* completely abolishes stalk formation in rich medium and leads
377 to the formation of wide cellular protrusions, named pseudostalks, under phosphate-limiting conditions
378 (Caccamo et al., 2020). Similar to the amorphous extensions observed for an *H. neptunium* Δ*bacAD* mu-
379 tant, these structures grow through disperse incorporation of new peptidoglycan and develop into viable
380 offspring. Their formation was also attributed to the entry of cell wall biosynthetic proteins into nascent
381 stalks (Caccamo et al., 2020), suggesting that the *H. neptunium* and *A. biprosthecum* BacA homologs share
382 the same barrier function during stalk formation. However, in *H. neptunium*, another layer of regulation
383 has been added in which bactofilins establish a second barrier close to the stalk tip that enables the
384 formation of stalk-terminal buds. Bud expansion requires the relocation of elongasome complexes from
385 the mother cell to the nascent bud at the onset of bud formation, as likely reflected by the fact that
386 components of the elongasome (MreB, RodZ) and new cell wall biosynthesis can be detected within the
387 stalk during a short interval at the end of the stalk elongation phase (Cserti et al., 2017). This process may
388 be facilitated by the (partial) disassembly of the bactofilin complex at the stalk base, but the mechanistic
389 details remain to be investigated. Another open question concerns the factors that control the dynamic
390 localization of bactofilin to the stalked pole and the future bud neck in the terminal segment of the stalk.
391 In *A. biprosthecum*, the recruitment of BacA assemblies to the sites of stalk biosynthesis is dependent on
392 the cell wall hydrolase SpmX (Caccamo et al., 2020). However, an *H. neptunium* mutant lacking this protein
393 shows normal morphology (Leicht et al., 2020), suggesting the existence of a different localization deter-
394 minant. The contribution of LmdC to bactofilin localization could not be investigated, because this protein
395 is essential for *H. neptunium* growth (Cserti et al., 2017). However, the apparently random positioning of
396 LmdC complexes in bactofilin-deficient cells suggests that its recruitment depends on the bactofilin cyto-
397 skeleton, excluding it as a potential candidate.

398 Intriguingly, bactofilins not only mediate stalk formation and stalk-terminal budding but also the forma-
399 tion of curved cell shapes. We show that both BacA and LmdC are required to establish the normal degree
400 of cell helicity in *R. rubrum*, with their absence leading to hyper-curved cells (**Figure 9C,D**). This result sug-
401 gests that the two proteins form an accessory module that counteracts the activity of a so-far unknown
402 system responsible for generating spiral cell shape in *R. rubrum* (**Figure 10B**). Cell curvature was shown to
403 promote cell motility (Martinez et al., 2016). It is tempting to speculate that the expression of *bacA* and
404 *lmdC* could be controlled in response to external cues to ensure optimal cell helicity and, thus, fitness in
405 different environments. Our results show that *R. rubrum* cells contain multiple BacA-LmdC complexes that
406 are distributed along the entire cell envelope but localize preferentially to the inner cell curvature (**Figure**
407 **9E**). In this case, it is immediately evident that BacA acts as a localization determinant for LmdC, since
408 LmdC is evenly dispersed in its absence (**Figure 9G**). To reduce cell helicity, the hydrolytic activity of LmdC
409 must ultimately stimulate the insertion of new peptidoglycan at the inner curvature, thereby increasing
410 the rate of cell elongation in this region and straightening the cell. A similar mechanism may also be at
411 work in the spirochete *L. biflexa*, where removal of the bactofilin paralog LbbD, whose gene lies adjacent
412 to a gene for putative M23 peptidase (LEPBI_I1430) (**Figure 3A**), was found to induce a strong increase in
413 cell helicity (Jackson et al., 2018). A different variation of this theme is found in *H. pylori*. There, the
414 bactofilin homolog CcmA also forms multiple assemblies along the cell envelope, which interact with a
415 membrane-spanning protein complex including an M23 peptidase (Csd1) homologous to LmdC (Sichel et
416 al., 2022; Taylor et al., 2020). However, these assemblies are enriched at the outer curvature, where they
417 stimulate peptidoglycan synthesis to locally increase the rate of cell elongation over that at the inner
418 curvature, leading to twisting of the cell body.

419 Notably, in all systems characterized so far in molecular detail, the function of bactofilin-M23 peptidase
420 complexes involves a stimulation of cell wall biosynthesis in a confined region of the cell envelope that
421 entails a local change in cell envelope curvature. In *H. neptunium*, these complexes are only localized to
422 narrow bands at the stalk base and bud neck, generating sharp bends at the transition zones between the
423 stalk and the adjacent mother cell and bud compartments. In spiral-shaped bacteria, by contrast, they are
424 scattered along the entire length of the cell, thereby establishing an elongated zone of increased longi-
425 tudinal growth that changes overall cell curvature. The same mechanistic principle may also explain the
426 morphogenetic role of bactofilins in so-far uninvestigated systems.

427 Collectively, our results underscore the role of bactofilins as versatile modulators of bacterial cell shape.
428 In association with M23 peptidases, they form cell wall biosynthetic complexes that introduce local

429 changes in cell envelope curvature. In doing so, they complement the activities of the tubulin and actin
430 cytoskeletons in cell shape determination and thus expand the morphogenetic potential of bacteria,
431 enabling the generation of complex cell shapes that go beyond the generic rod-like or spherical morpho-
432 logies. It will be interesting to investigate the molecular function of bactofilins in a range of morphologic-
433 ally diverse species to obtain a comprehensive picture of the functionalities provided by these cytoskeletal
434 proteins and the conservation of their mode of action.

Materials and methods

435 **Media and growth conditions**

436 *H. neptunium* LE670 (ATCC 15444) (Leifson, 1964) and its derivatives were grown in Artificial Sea Salt (ASS)
437 medium at 28 °C under aerobic conditions, shaking at 210 rpm in baffled flasks. ASS medium was
438 composed of 0.5% Bacto Peptone (Thermo Fisher Scientific, USA), 0.1% yeast extract, 1 mM $MgSO_4$,
439 0.5 mM $CaCl_2$ and 1.5% Instant Ocean Sea Salt (Spectrum Brands, USA), dissolved in deionized water. For
440 solid media, 1.5% agar was added prior to autoclaving. When appropriate, antibiotics were used at the
441 following concentrations (µg/mL in liquid/solid medium): rifampicin (1/2), kanamycin (100/200). The ex-
442 pression of genes under the control of the copper-inducible P_{Cu} promoter or the zinc-inducible P_{Zn}
443 promoter (Jung et al., 2015) was induced by the addition of $CuSO_4$ or $ZnSO_4$ to the concentrations
444 indicated in the text. To assess the growth of *H. neptunium*, cells were grown to exponential phase, diluted
445 in fresh medium to an optical density at 580 nm (OD_{580}) of 0.02, and transferred into 24-well polystyrene
446 microtiter plates (Becton Dickinson Labware, USA). Growth was then followed at 32 °C under double-
447 orbital shaking in an EPOCH 2 microplate reader (BioTek, USA) by measuring the OD_{580} at 20-min intervals.

448 *R. rubrum* S1 (ATCC 11170) (Molisch, 1907; Pfennig and Trüper, 1971; van Niel, 1944) and its derivatives
449 were grown in Bacto Tryptic Soy Broth (BD Diagnostic Systems, USA) at 28 °C under aerobic conditions,
450 shaking at 210 rpm in Erlenmeyer flasks. When appropriate, media were supplemented with antibiotics
451 at the following concentrations (µg/mL in liquid/solid medium): kanamycin (30/30), cefalexin (15/-).

452 *E. coli* strains were cultivated aerobically (shaking at 210 rpm) at 37 °C in LB medium. For plasmid-bearing
453 strains, antibiotics were added at the following concentrations (µg/mL in liquid/solid medium): kanamycin
454 (30/50), rifampicin (25/50), ampicillin (50/200). To grow *E. coli* WM3064, media were supplemented with
455 2,6-diaminopimelic acid (DAP) to a final concentration of 300 µM.

456 **Plasmid and strain construction**

457 The bacterial strains, plasmids, and oligonucleotides used in this study are listed in **Tables S3-S6**. *E. coli*
458 TOP10 (Thermo Fisher Scientific, USA) was used as host for cloning purposes. All plasmids were verified
459 by DNA sequencing. *H. neptunium* and *R. rubrum* were transformed by conjugation using the DAP-
460 auxotrophic strain *E. coli* WM3064 as a donor (Jung et al., 2015). The integration of non-replicating plas-
461 mids at the chromosomal P_{Cu} or P_{Zn} locus of *H. neptunium* was achieved by single homologous recombi-
462 nation (Jung et al., 2015). Gene replacement in *H. neptunium* and *R. rubrum* was achieved by double-

463 homologous recombination using the counter-selectable *sacB* marker (Cserti et al., 2017). Proper chromo-
464 somal integration or gene replacement was verified by colony PCR.

465 **Live-cell imaging**

466 Cells of *H. neptunium* and *R. rubrum* were grown to exponential phase in the appropriate medium and, if
467 suitable, induced with $CuSO_4$ prior to imaging. For depletion experiments, cells were grown in the pres-
468 ence of inducer, washed three times with inducer-free medium and then further cultivated in the absence
469 of inducer for the indicated period of time prior to analysis. To acquire still images, cells were transferred
470 onto 1% agarose pads (in water). For time-lapse analysis, cells were immobilized on pads made of 1%
471 agarose in ASS medium, and the cover slides were then sealed with VLAP (1:1:1 mixture of vaseline,
472 lanolin, and paraffin) to prevent dehydration. Imaging was performed using a Zeiss Axio Imager.M1
473 microscope equipped with a Zeiss alpha Plan-Apochromat 100x/1.40 Oil DIC objective and a pco.edge 3.1
474 sCMOS camera (PCO, Germany) or a Zeiss Axio Imager.Z1 microscope equipped with a Zeiss alpha Plan-
475 Apochromat 100x/1.46 Oil DIC M27 or a Plan-Apochromat 100x/1.40 Oil Ph3 M27 objective and a
476 pco.edge 4.2 sCMOS camera (PCO, Germany). An X-Cite 120PC metal halide light source (EXFO, Canada)
477 and ET-DAPI, ET-YFP or ET-TexasRed filter cubes (Chroma, USA) were used for fluorescence detection.
478 Microfluidic experiments were performed using a CellASIC ONIX EV262 Microfluidic System, equipped
479 with an F84 manifold and B04A microfluidic plates (Merck Millipore, Germany), which were flushed with
480 PBS buffer for 30 min before usage. Exponentially growing cells were flushed into the flow cells, cultivated
481 under continuous medium flow (0.4 ml/h), and imaged at regular intervals using the Axio Image.Z1 micros-
482 cope described above. To visualize sites of ongoing peptidoglycan synthesis, cells were grown to the
483 exponential phase, incubated for 1 min with 1 mM HADA and washed four times in ASS medium prior to
484 imaging.

485 Images were recorded with VisiView 3.3.0.6 (Visitron Systems, Germany) and processed with ImageJ
486 (Schneider et al., 2012) and Adobe Illustrator CS6 (Adobe Systems, USA). The subcellular distribution of
487 fluorescence signals was analyzed with BacStalk (Hartmann et al., 2020). Pearson's correlation coefficients
488 were determined using the JACoP plug-in (Bolte and Cordelieres, 2006) for ImageJ. Cell sinuosity was
489 determined using the ImageJ plug-in MicrobeJ (Ducret et al., 2016), with each analysis performed in
490 triplicate and 100 cells analyzed per strain and experiment. Results were displayed as SuperPlots (Lord et
491 al., 2020) generated using the SuperPlotsOfData web application (Goedhart, 2021). Pearson's correlation
492 coefficients were determined with ImageJ, using the "Align Fluorescence Channels" plugin (Norbert

493 Vischer, unpublished) to align the fluorescence images to be compared and then the JACoP plugin (Fabrice
494 P. Cordelières, unpublished) to determine the degree of colocalization.

495 **Single-particle tracking and diffusion analysis**

496 Cells were cultivated overnight in ASS medium, transferred into fresh medium and grown to exponential
497 phase prior to imaging by slimfield microscopy (Plank et al., 2009). In this approach, the back aperture of
498 the objective is underfilled by illumination with a collimated laser beam of reduced width, generating an
499 area of ~10 µm in diameter with a light intensity high enough to enable the visualization of single
500 fluorescent protein molecules at very high acquisition rates. The single-molecule level was reached by
501 bleaching of most molecules in the cell for 100 to 1,000 frames, followed by tracking of the remaining and
502 newly synthesized molecules for ~3,000 frames. Images were taken at 30 ms intervals using an Olympus
503 IX-71 microscope equipped with a UAPON 100x/ NA 1.49 TIRF objective, a back-illuminated electron-
504 multiplying charge-coupled device (EMCCD) iXon Ultra camera (Andor Solis, USA) in stream acquisition
505 mode, and a LuxX 457-100 (457 nm, 100 mW) light-emitting diode laser (Omicron-Laserage Laserprodukte
506 GmbH, Germany) as an excitation light source. The laser beam was focused onto the back focal plane and
507 operated during image acquisition with up to 2 mW (60 W/cm^2 at the image plane). Andor Solis 4.21
508 software was used for camera control and stream acquisition. Prior to analysis, frames recorded before
509 reaching the single-molecule level were removed from the streams, using photobleaching curves as a
510 reference. Subsequently, the streams were cropped to an equal length of 2,000 frames and the proper
511 pixel size (100 nm) and time increment were set in the imaging metadata using Fiji (Schindelin et al., 2012).
512 Single particles were tracked with u-track 2.2 (Jaqaman et al., 2008). Trajectories were only considered
513 for further statistical analysis if they had a length of at least five steps. Data analysis was performed using
514 SMTracker 2.0 (Oviedo-Bocanegra et al., 2021). An estimate of the diffusion coefficient and insight into
515 the kind of diffusive motion exhibited were obtained from mean-squared-displacement (MSD)-versus-
516 time-lag curves. In addition, the frame-to-frame displacements of all molecules in x and the y direction
517 were fitted to a two-population Gaussian mixture model to determine the proportions of mobile and static
518 molecules in each condition (Oviedo-Bocanegra et al., 2021).

519 **Transmission electron microscopy**

520 Images of *H. neptunium* cells, 10 µl of early exponential cell cultures were applied onto glow-discharged
521 electron microscopy grids (Formvar/Carbon Film on 300 Mesh Copper; Plano GmbH, Germany) and
522 incubated for 1 min at room temperature. The grid was manually blotted with Whatman filter paper to
523 remove excess liquid. Subsequently, the cells were negatively stained for 5 sec with 5 µl of 1% uranyl

524 acetate. After three washes with H_2O, the grids were dried and imaged in a 100 kV JEM-1400 Plus trans-
525 mission electron microscope (JEOL, USA). To image BacA polymers, purified BacA-His_6 was dialyzed against
526 low-salt buffer (50 mM HEPES pH 7.2, 10 mM NaCl, 5 mM $MgCl_2$, 0.1 mM EDTA, 1 mM ß-mercaptoethanol)
527 for 16 h. The protein was spotted onto carbon-coated grids and allowed to settle for 2 min. The grids were
528 blotted dry, stained with 1:2 diluted supernatant of saturated 2 % uranyl acetate (in H_2O) for 1 min, dried
529 and imaged using a Zeiss CEM902 electron microscope, operated at 80 kV and equipped with a 2048x2048
530 pixel CCD camera. Image processing was carried out using Photoshop CS2 and Illustrator CS5 (Adobe
531 Systems, USA).

532 **Immunoblot analysis**

533 Antibodies against BacA were raised by immunization of rabbits with purified BacA-His_6 protein
534 (Eurogentec, Belgium). Cells were harvested in the exponential growth phase. Immunoblot analysis was
535 conducted as described previously (Thanbichler and Shapiro, 2006), using anti-BacA antiserum (1:10.000),
536 a monoclonal anti-mNeonGreen antibody (Chromotek, Germany; Cat. #: 32f6; RRID: AB_2827566), a
537 polyclonal anti-GFP antibody (Sigma, Germany; Cat. #: G1544; RRID: AB_439690) or a polyclonal anti-
538 mCherry antibody (BioVision, USA; Cat. #: 5993; RRID: AB_1975001) at dilutions of 1:10,000, 1:1,000,
539 1:10,000 or 1:10,000, respectively. Goat anti-rabbit immunoglobulin G conjugated with horse-radish per-
540 oxidase (Perkin Elmer, USA) was used as secondary antibody. Immunocomplexes were detected with the
541 Western Lightning Plus-ECL chemiluminescence reagent (Perkin Elmer, USA). The signals were recorded
542 with a ChemiDoc MP imaging system (BioRad, Germany) and analyzed using Image Lab software (BioRad,
543 Germany).

544 **Peptidoglycan analysis**

545 Cultures of exponentially growing cells of the *H. neptunium* wild type and its mutant derivatives EC28
546 (Δ*bacA*), EC23 (Δ*bacD*) and EC33 (Δ*bacAD*) were rapidly cooled to 4°C and harvested by centrifugation at
547 16,000 ×g for 30 min. The cells were resuspended in 6 ml of ice-cold H_2O and added dropwise to 6 ml of a
548 boiling solution of 8% sodium dodecylsulfate (SDS) that was stirred vigorously. After 30 min of boiling, the
549 suspension was cooled to room temperature. Peptidoglycan was isolated from the cell lysates as
550 described previously (Glauner, 1988) and digested with the muramidase cellosyl (kindly provided by
551 Hoechst, Frankfurt, Germany). The resulting muropeptides were reduced with sodium borohydride and
552 separated by HPLC following an established protocol (Bui et al., 2009; Glauner, 1988). The identity of
553 eluted fragments was assigned based on the known retention times of muropeptides, as reported
554 previously (Cserti et al., 2017; Glauner, 1988).

555 **LmdC enzymatic activity assay**

556 To test the enzymatic activity of LmdC, peptidoglycan from *E. coli* D456 (Edwards and Donachie, 1993)
557 was mixed with 10 µM LmdC in buffer A (20 mM Hepes/NaOH pH 7.5, 50 mM NaCl, 1 mM $ZnCl_2$) or buffer
558 B (20 mM sodium acetate pH 5.0, 50 mM NaCl, 1 mM $ZnCl_2$) in a final volume of 50 µL and incubated at
559 37°C for 16 h in a thermal shaker set at 900 rpm. A mixture of peptidoglycan in buffer B without LmdC was
560 used as a control. The reactions were stopped by heating at 100°C for 10 min. The peptidoglycan was then
561 further digested overnight with cellosyl, and the reactions were stopped by heating at 100°C for 10 min.
562 After centrifugation of the samples at 14,000 rpm for 10 min, the supernatants were recovered, reduced
563 with sodium borohydride, acidified to pH 4.0 – pH 4.5 with dilute 20% phosphoric acid and subjected to
564 HPLC analysis as previously described (Glauner, 1988).

565 **Bio-layer interferometry**

566 Bio-layer interferometry analyses were conducted using a BLItz system equipped with High Precision
567 Streptavidin (SAX) Biosensors (Sartorius, Germany). As a ligand, a custom-synthetized N-terminally biotin-
568 ylated peptide comprising residues Met1 to Gln38 of LmdC (GenScript, USA) was immobilized on the
569 biosensors. After the establishment of a stable baseline, association reactions were monitored at various
570 analyte concentrations. At the end of each binding step, the sensor was transferred into an analyte-free
571 buffer to follow the dissociation kinetics. The extent of non-specific binding was assessed by monitoring
572 the interaction of analyte with unmodified sensors. All analyses were performed in BLItz binding buffer
573 (25 mM HEPES/KOH pH 7.6, 100 mM KCl, 10 mM $MgSO_4$, 1 mM DTT, 10 mM BSA, 0.01% Tween).

574 **Protein purification**

575 To purify BacA-His_6, *E. coli* Rosetta(DE3)pLysS (Invitrogen) was transformed with pEC86 and grown in LB
576 medium at 37 °C to an OD_{600} of 0.8. Isopropyl-β-D-1-thiogalactopyranoside (IPTG) was added to a final
577 concentration of 0.5 mM and the incubation was continued for another 3 h. The cells were harvested by
578 centrifugation for 15 min at 7,500 ×g and 4 °C and washed with buffer B2 (50 mM NaH_2PO_4, 300 mM NaCl,
579 10 mM imidazole, adjusted to pH 8.0 with NaOH). Subsequently, they were resuspended in buffer B2
580 containing 100 µg/mL phenylmethylsulfonyl fluoride, 10 µg/mL DNase I and 1 mM β-mercaptoethanol
581 and lysed by three passages through a French press at 16,000 psi. After the removal of cell debris by
582 centrifugation at 30,000 ×g for 30 min, the supernatant was applied onto a 5 mL HisTrap HP column (GE
583 Healthcare) equilibrated with buffer B3 (50 mM NaH_2PO_4, 300 mM NaCl, 20 mM imidazole, adjusted to
584 pH 8.0 with NaOH). The column was washed with 10 column volumes (CV) of the same buffer, and protein
585 was eluted at a flow rate of 1 mL/min with a linear imidazole gradient obtained by mixing buffers B3 and

586 B4 (50 mM NaH_2PO_4, 300 mM NaCl, 250 mM imidazole, adjusted to pH 8.0 with NaOH). Fractions
587 containing high concentrations of BacA-His_6 were pooled and dialyzed against 3 L of buffer B5 (20 mM
588 Tris/HCl pH 8.0, 10 mM NaCl, 1 mM β-mercaptoethanol) at 4 °C. After the removal of precipitates by
589 centrifugation at 30,000 ×g for 30 min, the protein solution was aliquotted and snap-frozen in liquid
590 nitrogen. Aliquots were stored at -80 °C until further use.

591 To purify LmdC, the protein was first produced as a His_6-SUMO-LmdC fusion (Marblestone et al., 2006).
592 To this end, *E. coli* Rosetta(DE3)pLysS cells carrying plasmid pLY015 were grown at 37 °C in 3 L of LB
593 medium supplemented with ampicillin and chloramphenicol. At an OD_{600} of 0.6, the culture was chilled to
594 18°C, and protein synthesis was induced by the addition of 1 mM IPTG prior to overnight incubation at 18
595 °C. The cultures were harvested by centrifugation at 10,000 ×g for 20 min at 4 °C and washed with lysis
596 buffer (50 mM Tris/HCl pH 8.0, 300 mM NaCl). Cells were resuspended in lysis buffer supplemented with
597 5 mM imidazole, 10 mg/mL DNase I and 100 mg/mL PMSF. After three passages through a French press
598 (16,000 psi), the cell lysate was clarified by centrifugation (30,000 ×g, 30 min, 4 °C). Protein was then
599 purified using zinc-affinity chromatography using a 1 mL Zn-NTA column (Cube Biotech) equilibrated with
600 lysis buffer containing 5 mM imidazole. Protein was eluted with a linear gradient of 5 to 250 mM imidazole
601 in lysis buffer at a flow rate of 1 mL/min. Fractions containing high concentrations of His_6-SUMO-LmdC
602 were pooled and dialyzed against 3 L of low-salt lysis buffer (20 mM Tris/HCl pH 7.6, 50 mM NaCl, 10%
603 (v/v) glycerol). After the addition of Ulp1 protease (Marblestone et al., 2006) and dithiothreitol (1 mM),
604 the protein was incubated for 4 h at 4 °C to cleave off the His_6-SUMO tag. The solution was centrifuged
605 for 30 min at 38,000 ×g and 4 °C to remove precipitates and then subjected to ion exchange chromato-
606 graphy using a 1 mL HiTrap Q HP column (Cytiva, USA) equilibrated with low-salt lysis buffer. His_6-SUMO
607 passed the column in the flow-through, and LmdC was eluted with a linear gradient of 150-1000 mM NaCl
608 in low-salt buffer. Fractions containing LmdC were concentrated in an Amicon Ultra-4 10K spin
609 concentrator (MWCO 10,000; Merck, Germany). After the removal of precipitates by centrifugation at
610 30,000 ×g for 30 min, LmdC was further purified by size exclusion chromatography (SEC) on a HighLoad
611 16/60 Superdex 200 pg column (GE Healthcare, USA) equilibrated with SEC buffer (20 mM Tris/HCl pH 7.4,
612 150 mM NaCl). Fractions containing pure protein were pooled and concentrated. After the removal of
613 precipitates by centrifugation at 30,000 ×g, the protein solution was snap-frozen in liquid N_2 and stored
614 at -80 °C until further use.

615 **Bioinformatic analysis**

616 Protein similarity searches were performed with BLAST (Altschul et al., 1990), using the BLAST server of
617 the National Institutes of Health (https://blast.ncbi.nlm.nih.gov/Blast.cgi). Transmembrane helices were
618 predicted with DeepTMHMM (Hallgren et al., 2022), coiled-coil regions with PCOILS (Lupas, 1996). The
619 positions of conserved functional domains were determined using the PFAM server (Mistry et al., 2021).
620 AlphaFold2 (Jumper et al., 2021) and AlphaFold-Multimer (Evans et al., 2022), as implemented in the
621 AlphaFold.ipynb notebook on Google Colab, were used to predict the tertiary or quaternary structure of
622 proteins, respectively. SuperPlots (Lord et al., 2020) were used to visualize cell length distributions and to
623 evaluate the statistical significance of differences between multiple distributions, employing the
624 PlotsOfData web app (Postma and Goedhart, 2019).

Acknowledgements

We thank Julia Rosum for excellent technical assistance, Ying Liu for help with the construction of plasmids, Daniela Vollmer for the purification of peptidoglycan, and Maria Perez-Burgos and Lotte Søgaard-Andersen for help with the transmission electron microscopy analyses. This work was supported by the University of Marburg (core funding to P.G. and M.T.), the Max Planck Society (Max Planck Fellowship to M.T.), the German Research Foundation (DFG; project 450420164 to M.T. and project 26942323 – TRR 174 to P.L.G.), and and the United Kingdom Biotechnology and Biological Sciences Research Council (grant BB/W013630/1 to W.V.). M.O.V. was a fellow of the International Max Planck Research School for Environmental, Cellular and Molecular Microbiology (IMPRS-Mic).

Data availability

All relevant data generated in this study are included in the manuscript and the supplemental information.

Author contributions

M.O.V., E.C. and M.T. conceived the study. M.O.V., E.C. and S.P. constructed plasmids and strains and performed the growth analyses and subcellular localization studies. M.O.V. purified proteins and conducted the biochemical studies. P.S. analyzed the co-conservation of BacA and LmdC homologs. J.B. conducted the peptidoglycan analysis. R.H.-T. performed the single-particle tracking analysis. M.O.V., E.C., S.P. R.H.-T., P.S., J.B., W.V. and M.T. analyzed the data. W.V., P.L.G. and M.T. supervised the study. W.V., P.L.G. and M.T. secured funding. M.O.V. and M.T. wrote the paper, with input from all other authors.

Competing interests

The authors declare no competing interests.

References

634 Aaron M, Charbon G, Lam H, Schwarz H, Vollmer W, Jacobs-Wagner C. 2007. The tubulin homologue FtsZ
635 contributes to cell elongation by guiding cell wall precursor synthesis in *Caulobacter crescentus*.
636 *Molecular Microbiology* **64**:938-952.

637 Altschul SF, Gish W, Miller W, Myers EW, Lipman DJ. 1990. Basic local alignment search tool. *Journal of*
638 *Molecular Biology* **215**:403-410.

639 Badger JH, Hoover TR, Brun YV, Weiner RM, Laub MT, Alexandre G, Mrazek J, Ren Q, Paulsen IT, Nelson
640 KE *et al.* 2006. Comparative genomic evidence for a close relationship between the dimorphic
641 prosthecate bacteria *Hyphomonas neptunium* and *Caulobacter crescentus*. *Journal of Bacteriology*
642 **188**:6841-6850.

643 Bolte S, Cordelieres FP. 2006. A guided tour into subcellular colocalization analysis in light microscopy.
644 *Journal of Microscopy* **224**:213-232.

645 Brown PJ, Kysela DT, Brun YV. 2011. Polarity and the diversity of growth mechanisms in bacteria. *Seminars*
646 *in Cell & Developmental Biology* **22**:790-798.

647 Bui NK, Gray J, Schwarz H, Schumann P, Blanot D, Vollmer W. 2009. The peptidoglycan sacculus of
648 *Myxococcus xanthus* has unusual structural features and is degraded during glycerol-induced
649 myxospore development. *Journal of Bacteriology* **191**:494-505.

650 Caccamo PD, Jacq M, VanNieuwenhze MS, Brun YV. 2020. A division of labor in the recruitment and
651 topological organization of a bacterial morphogenic complex. *Current Biology* **30**:3908-3922.

652 Cserti E, Rosskopf S, Chang YW, Eisheuer S, Selter L, Shi J, Regh C, Koert U, Jensen GJ, Thanbichler M. 2017.
653 Dynamics of the peptidoglycan biosynthetic machinery in the stalked budding bacterium *Hyphomonas*
654 *neptunium*. *Molecular Microbiology* **103**:875-895.

655 Deng X, Gonzalez Llamazares A, Wagstaff JM, Hale VL, Cannone G, McLaughlin SH, Kureisaite-Ciziene D,
656 Löwe J. 2019. The structure of bactofilin filaments reveals their mode of membrane binding and lack
657 of polarity. *Nature Microbiology* **4**:2357-2368.

658 Ducret A, Quardokus EM, Brun YV. 2016. MicrobeJ, a tool for high throughput bacterial cell detection and
659 quantitative analysis. *Nature Microbiology* **1**:16077.

660 Edwards D, Donachie WD. 1993. Construction of a triple deletion of penicillin-binding proteins 4, 5, and 6
661 in *Escherichia coli*. In: Bacterial growth and lysis, eds: de Pedro M, Höltje J-V, Löffelhardt W (New York
662 and London: Plenum Press), pp. 369–374.

663 Egan AJF, Errington J, Vollmer W. 2020. Regulation of peptidoglycan synthesis and remodelling. *Nature*
664 *Reviews Microbiology* **18**:446-460.

665 Evans R, O'Neill M, Pritzel A, Antropova N, Senior A, Green T, Žídek A, Bates R, Blackwell S, Yim J *et al.*
666 2022. Protein complex prediction with AlphaFold-Multimer. bioRxiv, DOI:
667 10.1101/2021.1110.1104.463034

668 Figueroa-Cuilan WM, Randich AM, Dunn CM, Santiago-Collazo G, Yowell A, Brown PJB. 2021. Diversifi-
669 cation of LytM protein functions in polar elongation and cell division of *Agrobacterium tumefaciens*.
670 *Frontiers in Microbiology* **12**:729307.

671 Firczuk M, Mucha A, Bochtler M. 2005. Crystal structures of active LytM. *Journal of Molecular Biology*
672 **354**:578-590.

673 Glauner B. 1988. Separation and quantification of muropeptides with high-performance liquid chromato-
674 graphy. *Analytical Biochemistry* **172**:451-464.

675 Goedhart J. 2021. SuperPlotsOfData – a web app for the transparent display and quantitative comparison
676 of continuous data from different conditions. *Molecular Biology of the Cell* **32**:470-474.

677 Goley ED, Comolli LR, Fero KE, Downing KH Shapiro, L. 2010. DipM links peptidoglycan remodelling to
678 outer membrane organization in *Caulobacter*. *Molecular Microbiology* **77**:56-73.
679 Grabowska M, Jagielska E, Czapinska H, Bochtler M, Sabala I. 2015. High resolution structure of an M23
680 peptidase with a substrate analogue. *Scientific Reports* **5**:14833.
681 Gurnani Serrano CK, Winkle M, Martorana AM, Biboy J, More N, Moynihan P, Banzhaf M, Vollmer W,
682 Polissi A. 2021. ActS activates peptidoglycan amidases during outer membrane stress in *Escherichia*
683 *coli*. *Molecular Microbiology* **116**:329-342.
684 Hallgren J, Tsirigos KD, Pedersen MD, Almagro Armenteros JJ, Marcatili P, Nielsen H, Krogh A, Winther O.
685 2022. DeepTMHMM predicts alpha and beta transmembrane proteins using deep neural networks.
686 bioRxiv, DOI: 10.1101/2022.04.08.487609
687 Hartmann R, van Teeseling MCF, Thanbichler M, Drescher K. 2020. BacStalk: A comprehensive and
688 interactive image analysis software tool for bacterial cell biology. *Molecular Microbiology* **114**:140-150.
689 Hay NA, Tipper DJ, Gygi D, Hughes C. 1999. A novel membrane protein influencing cell shape and multi-
690 cellular swarming of *Proteus mirabilis*. *Journal of Bacteriology* **181**:2008-2016.
691 Hughes HV, Lisher JP, Hardy GG, Kysela DT, Arnold RJ, Giedroc DP, Brun YV. 2013. Co-ordinate synthesis
692 and protein localization in a bacterial organelle by the action of a penicillin-binding-protein. *Molecular*
693 *Microbiology* **90**:1162-1177.
694 Hussain S, Wivagg CN, Szwedziak P, Wong F, Schaefer K, Izore T, Renner LD, Holmes MJ, Sun Y, Bisson-
695 Filho AW*, et al.* 2018. MreB filaments align along greatest principal membrane curvature to orient cell
696 wall synthesis. *Elife* **7**:e32471.
697 Jackson KM, Schwartz C, Wachter J, Rosa PA, Stewart PE. 2018. A widely conserved bacterial cytoskeletal
698 component influences unique helical shape and motility of the spirochete *Leptospira biflexa*. *Molecular*
699 *Microbiology* **108**:77-89.
700 Jaqaman K, Loerke D, Mettlen M, Kuwata H, Grinstein S, Schmid SL, Danuser G. 2008. Robust single-
701 particle tracking in live-cell time-lapse sequences. *Nature Methods* **5**:695-702.
702 Jumper J, Evans R, Pritzel A, Green T, Figurnov M, Ronneberger O, Tunyasuvunakool K, Bates R, Zidek A,
703 Potapenko A*, et al.* 2021. Highly accurate protein structure prediction with AlphaFold. *Nature* **596**:583-
704 589.
705 Jung A, Eisheuer S, Cserti E, Leicht O, Strobel W, Möll A, Schlimpert S, Kühn J, Thanbichler M. 2015.
706 Molecular toolbox for genetic manipulation of the stalked budding bacterium *Hyphomonas neptunium*.
707 *Applied and Environmental Microbiology* **81**:736-744.
708 Jung A, Rassbach A, Pulpetta RL, van Teeseling MCF, Heinrich K, Sobetzko P, Serrania J, Becker A,
709 Thanbichler M. 2019. Two-step chromosome segregation in the stalked budding bacterium
710 *Hyphomonas neptunium*. *Nature Communications* **10**:3290.
711 Klein EA, Schlimpert S, Hughes V, Brun YV, Thanbichler M, Gitai Z. 2013. Physiological role of stalk
712 lengthening in *Caulobacter crescentus*. *Communicative & Integrative Biology* **6**:e24561.
713 Koch MK, McHugh CA, Hoiczyk E. 2011. BacM, an N-terminally processed bactofilin of *Myxococcus*
714 *xanthus*, is crucial for proper cell shape. *Molecular Microbiology* **80**:1031-1051.
715 Kühn J, Briegel A, Mörschel E, Kahnt J, Leser K, Wick S, Jensen GJ, Thanbichler M. 2010. Bactofilins, a
716 ubiquitous class of cytoskeletal proteins mediating polar localization of a cell wall synthase in
717 *Caulobacter crescentus*. *EMBO Journal* **29**:327-339.
718 Kuru E, Tekkam S, Hall E, Brun YV, Van Nieuwenhze MS. 2015. Synthesis of fluorescent D-amino acids and
719 their use for probing peptidoglycan synthesis and bacterial growth *in situ*. *Nature Protocols* **10**:33-52.
720 Kysela DT, Randich AM, Caccamo PD, Brun YV. 2016. Diversity takes shape: understanding the mechanistic
721 and adaptive basis of bacterial morphology. *PLoS Biology* **14**:e1002565.

722 Leicht O, van Teeseling MCF, Panis G, Reif C, Wendt H, Viollier PH, Thanbichler M. 2020. Integrative and
723 quantitative view of the CtrA regulatory network in a stalked budding bacterium. *PLoS Genetics*
724 **16**:e1008724.
725 Leifson E. 1964. *Hyphomicrobium neptunium sp. n*. *Antonie Van Leeuwenhoek* **30**:249-256.
726 Letunic I, Bork P. 2021. Interactive Tree Of Life (iTOL) v5: an online tool for phylogenetic tree display and
727 annotation. *Nucleic Acids Research* **49**:W293-W296.
728 Lin L, Osorio Valeriano M, Harms A, Søgaard-Andersen L, Thanbichler M. 2017. Bactofilin-mediated
729 organization of the ParAB*S* chromosome segregation system in *Myxococcus xanthus*. *Nature*
730 *Communications* **8**:1817.
731 Lord SJ, Velle KB, Mullins RD, Fritz-Laylin LK. 2020. SuperPlots: Communicating reproducibility and
732 variability in cell biology. *Journal of Cell Biology* **219**:e202001064.
733 Lupas A. 1996. Prediction and analysis of coiled-coil structures. *Methods in Enzymology* **266**:513-525.
734 Marblestone JG, Edavettal SC, Lim Y, Lim P, Zuo X, Butt TR. 2006. Comparison of SUMO fusion technology
735 with traditional gene fusion systems: enhanced expression and solubility with SUMO. *Protein Science*
736 **15**:182-189.
737 Margolin W. 2009. Sculpting the bacterial cell. *Current Biology* **19**:R812-R822.
738 Martinez LE, Hardcastle JM, Wang J, Pincus Z, Tsang J, Hoover TR, Bansil R, Salama NR. 2016. *Helicobacter*
739 *pylori* strains vary cell shape and flagellum number to maintain robust motility in viscous environments.
740 *Molecular Microbiology* **99**:88-110.
741 McQuillen R, Xiao J. 2020. Insights into the structure, function, and dynamics of the bacterial cytokinetic
742 FtsZ-ring. *Annual Review of Biophysics* **49**:309-341.
743 Mistry J, Chuguransky S, Williams L, Qureshi M, Salazar GA, Sonnhammer ELL, Tosatto SCE, Paladin L, Raj
744 S, Richardson LJ*, et al.* 2021. Pfam: The protein families database in 2021. *Nucleic Acids Research*
745 **49**:D412-D419.
746 Molisch H. 1907. Die Purpurbakterien nach neuen Untersuchungen (Jena: Gustav Fischer).
747 Möll A, Schlimpert S, Briegel A, Jensen GJ, Thanbichler M. 2010. DipM, a new factor required for
748 peptidoglycan remodelling during cell division in *Caulobacter crescentus*. *Molecular Microbiology*
749 **77**:90-107.
750 Moore RL. 1981. The biology of *Hyphomicrobium* and other prosthecate, budding bacteria. *Annual Review*
751 *of Microbiology* **35**:567-594.
752 Munk AC, Copeland A, Lucas S, Lapidus A, Del Rio TG, Barry K, Detter JC, Hammon N, Israni S, Pitluck S *et*
753 *al.* 2011. Complete genome sequence of *Rhodospirillum rubrum* type strain (S1). *Standards in Genomic*
754 *Sciences* **4**:293-302.
755 Oviedo-Bocanegra LM, Hinrichs R, Rotter DAO, Dersch S, Graumann PL. 2021. Single molecule/particle
756 tracking analysis program SMTracker 2.0 reveals different dynamics of proteins within the RNA
757 degradosome complex in *Bacillus subtilis*. *Nucleic Acids Research* **49**:e112.
758 Paysan-Lafosse T, Blum M, Chuguransky S, Grego T, Pinto BL, Salazar GA, Bileschi ML, Bork P, Bridge A,
759 Colwell L *et al.* 2022. InterPro in 2022. *Nucleic Acids Research* **51**:D418-D427.
760 Persat A, Stone HA, Gitai Z. 2014. The curved shape of *Caulobacter crescentus* enhances surface
761 colonization in flow. *Nature Communications* **5**:3824.
762 Pfennig N, Trüper HG. 1971. Type and neotype strains of the species of phototrophic bacteria maintained
763 in pure culture. *International Journal of Systematic Bacteriology* **21**:19-24.
764 Plank M, Wadhams GH, Leake MC. 2009. Millisecond timescale slimfield imaging and automated
765 quantification of single fluorescent protein molecules for use in probing complex biological processes.
766 *Integrative Biology (Camb)* **1**:602-612.

767 Poggio S, Takacs CN, Vollmer W, Jacobs-Wagner C. 2010. A protein critical for cell constriction in the Gram-
768 negative bacterium *Caulobacter crescentus* localizes at the division site through its peptidoglycan-
769 binding LysM domains. *Molecular Microbiology* **77**:74-89.

770 Postma M, Goedhart J. 2019. PlotsOfData—A web app for visualizing data together with their summaries.
771 *PLOS Biology* **17**:e3000202.

772 Randich AM, Brun YV. 2015. Molecular mechanisms for the evolution of bacterial morphologies and
773 growth modes. *Frontiers in Microbiology* **6**:580.

774 Rohs PDA, Bernhardt TG. 2021. Growth and division of the peptidoglycan matrix. *Annual Review of*
775 *Microbiology* **75**:315-336.

776 Schindelin J, Arganda-Carreras I, Frise E, Kaynig V, Longair M, Pietzsch T, Preibisch S, Rueden C, Saalfeld S,
777 Schmid B *et al.* 2012. Fiji: an open-source platform for biological-image analysis. *Nature Methods*
778 **9**:676-682.

779 Schneider CA, Rasband WS, Eliceiri KW. 2012. NIH Image to ImageJ: 25 years of image analysis. *Nature*
780 *Methods* **9**:671-675.

781 Shaner NC, Campbell RE, Steinbach PA, Giepmans BN, Palmer AE, Tsien RY. 2004. Improved monomeric
782 red, orange and yellow fluorescent proteins derived from Discosoma sp. red fluorescent protein.
783 *Nature Biotechnology* **22**:1567-1572.

784 Shaner NC, Lambert GG, Chammas A, Ni Y, Cranfill PJ, Baird MA, Sell BR, Allen JR, Day RN, Israelsson M *et*
785 *al.* 2013. A bright monomeric green fluorescent protein derived from *Branchiostoma lanceolatum*.
786 *Nature Methods* **10**:407-409.

787 Shi C, Fricke P, Lin L, Chevelkov V, Wegstroth M, Giller K, Becker S, Thanbichler M, Lange A. 2015. Atomic-
788 resolution structure of cytoskeletal bactofilin by solid-state NMR. *Science Advances* **1**:e1501087.

789 Shi H, Bratton BP, Gitai Z, Huang KC. 2018. How to Build a bacterial cell: MreB as the foreman of *E. coli*
790 construction. *Cell* **172**:1294-1305.

791 Sichel SR, Bratton BP, Salama NR. 2022. Distinct regions of *H. pylori*'s bactofilin CcmA regulate protein-
792 protein interactions to control helical cell shape. *Elife* **11**:e80111.

793 Sycuro LK, Pincus Z, Gutierrez KD, Biboy J, Stern CA, Vollmer W, Salama NR. 2010. Peptidoglycan
794 crosslinking relaxation promotes *Helicobacter pylori*'s helical shape and stomach colonization. *Cell*
795 **141**:822-833.

796 Taylor JA, Bratton BP, Sichel SR, Blair KM, Jacobs HM, DeMeester KE, Kuru E, Gray J, Biboy J,
797 VanNieuwenhze MS *et al.* 2020. Distinct cytoskeletal proteins define zones of enhanced cell wall
798 synthesis in *Helicobacter pylori*. *Elife* **9**:e52482.

799 Taylor JA, Sichel SR, Salama NR. 2019. Bent bacteria: A comparison of cell shape mechanisms in
800 proteobacteria. *Annual Review of Microbiology* **73**:457-480.

801 Thanbichler M, Shapiro L. 2006. MipZ, a spatial regulator coordinating chromosome segregation with cell
802 division in *Caulobacter*. *Cell* **126**:147-162.

803 Typas A, Banzhaf M, Gross CA, Vollmer W. 2012. From the regulation of peptidoglycan synthesis to
804 bacterial growth and morphology. *Nature Reviews Microbiology* **10**:123-136.

805 Uehara T, Parzych KR, Dinh T, Bernhardt TG. 2010. Daughter cell separation is controlled by cytokinetic
806 ring-activated cell wall hydrolysis. *EMBO Journal* **29**:1412-1422.

807 van Niel CB. 1944. The culture, general physiology, morphology, and classification of the non-sulfur purple
808 and brown bacteria. *Bacteriological Reviews* **8**:1-118.

809 van Teeseling MCF, de Pedro MA, Cava F. 2017. Determinants of bacterial morphology: from fundamen-
810 tals to possibilities for antimicrobial targeting. *Frontiers in Microbiology* **8**:1264.

811 Varadi M, Anyango S, Deshpande M, Nair S, Natassia C, Yordanova G, Yuan D, Stroe O, Wood G, Laydon A
812 *et al.* 2022. AlphaFold Protein Structure Database: massively expanding the structural coverage of
813 protein-sequence space with high-accuracy models. *Nucleic Acids Research* **50**:D439-D444.
814 Vasa S, Lin L, Shi C, Habenstein B, Riedel D, Kühn J, Thanbichler M, Lange A. 2015. β-Helical architecture
815 of cytoskeletal bactofilin filaments revealed by solid-state NMR. *Proceedings of the National Academy*
816 *of Sciences U S A* **112**:E127-136.
817 Vollmer W, Blanot D, de Pedro MA. 2008. Peptidoglycan structure and architecture. *FEMS Microbiology*
818 *Reviews* **32**:149-167.
819 Wagner JK, Brun YV. 2007. Out on a limb: how the *Caulobacter* stalk can boost the study of bacterial cell
820 shape. *Molecular Microbiology* **64**:28-33.
821 Wali TM, Hudson GR, Danald DA, Weiner RM. 1980. Timing of swarmer cell cycle morphogenesis and
822 macromolecular synthesis by *Hyphomicrobium neptunium* in synchronous culture. *Journal of*
823 *Bacteriology* **144**:406-412.
824 Wong F, Garner EC, Amir A. 2019. Mechanics and dynamics of translocating MreB filaments on curved
825 membranes. *Elife* **8**:e40472.
826 Yang DC, Blair KM, Salama NR. 2016. Staying in shape: the impact of cell shape on bacterial survival in
827 diverse environments. *Microbiology and Molecular Biology Reviews* **80**:187-203.
828 Zuckerman DM, Boucher LE, Xie K, Engelhardt H, Bosch J, Hoiczyk E. 2015. The bactofilin cytoskeleton
829 protein BacM of *Myxococcus xanthus* forms an extended beta-sheet structure likely mediated by
830 hydrophobic interactions. *PLoS One* **10**:e0121074.

831 ## Figure legends

832 **Figure 1. Bactofilin BacA is required for proper cell morphology in *H. neptunium*. (A)** Schematic repre-
833 sentation of the two bactofilin genes present in the *H. neptunium* genome. *bacA* lies adjacent to the M23
834 peptidase gene *lmdC*. Arrows indicate the direction of transcription. **(B)** Domain organization of BacA and
835 BacD from *H. neptunium*. The bactofilin polymerization domain (colored boxes) is flanked by non-struc-
836 tured N- and C-terminal regions. **(C)** Morphology of *H. neptunium* bactofilin mutants. Shown are represen-
837 tative cells of strains LE670 (wild type), EC28 (Δ*bacA*), EC23 (Δ*bacD*) and EC33 (Δ*bacAD*), imaged by
838 differential interference contrast (DIC) microscopy. Bar: 4 µm. **(D)** Immunoblot analysis of the strains
839 shown in panel C, performed using anti-BacA antibodies. **(E)** Transmission electron micrographs of Δ*bacA*
840 cells at the early stalked-cell stage. Bar: 1 µm. **(F)** Quantification of the proportion of phenotypically ab-
841 normal stalked and budding cells in cultures of the strains analyzed in panel C (n = 100 cells per strain).

842 **Figure 1—figure supplement 1. The dimorphic lifecycle of *H. neptunium*.** A motile, flagellated swimmer
843 sheds its flagellum and forms a stalk at the opposite cell pole. A a defined point in the cell cycle, the
844 terminal segment of the stalk dilates and develops into a new swimmer cell. After cell division, the new-
845 born swimmer cell first needs to differentiate into a stalked cell to initiate a new round of cell division,
846 whereas the stalked mother cell immediately enters the next replication cycle. The predominant growth
847 zones (Cserti et al., 2017) are indicated in red.

848 **Figure 1—figure supplement 2. Phenotypic analysis of *H. neptunium* bactofilin mutants. (A)** Immunoblot
849 analysis of strains LE670 (wild type), EC28 (Δ*bacA*) and EC41 (Δ*bacA* P_{Cu}::P_{Cu}-*bacA*) grown in the absence
850 (-*bacA*) and presence (+*bacA*) of 0.5 mM $CuSO_4$, performed with an anti-BacA antibody. **(B)** Rescue of the
851 phenotype of a Δ*bacA* mutant by ectopic expression of *bacA*. Cells of strain EC41 (Δ*bacA* P_{Cu}::P_{Cu}-*bacA*)
852 were grown in copper-free medium, induced by the addition of copper, and imaged after the indicated
853 time incubation times. Bar: 3 µm. **(C)** Quantification of the proportion of phenotypically abnormal stalked
854 and budding cells in the cultures of strains EC41 (Δ*bacA* P_{Cu}::P_{Cu}-*bacA*) and EC43 (Δ*bacA* P_{Zn}::P_{Zn}-*bacD*)
855 analyzed in panels B and E before (t=0 h) and 24 h after induction (n = 100 cells per time point). **(D)** Trans-
856 mission electron micrographs of Δ*bacD* cells at the swimmer and stalk cell stage. Bar: 1 µm. **(E)** DIC images
857 of a Δ*bacA* mutant overproducing BacD from a zinc-inducible promoter. Cells of strain EC43 (Δ*bacA*
858 P_{Zn}::P_{Zn}-*bacD*) were grown in inducer-free medium, induced by the addition of 0.5 mM $ZnSO_4$, and imaged
859 after the indicated incubation times. Bar: 3 µm.

860 **Figure 2. Lack of BacA leads to uncontrolled growth of the stalk and bud compartments. (A)** Immunoblot
861 showing the levels of BacA in strain EC41 (Δ*bacA* P_{Cu}-*bacA*) over the course of BacA depletion. Cells were

862 grown in copper-containing medium, washed and transferred to inducer-free medium. At the indicated
863 time points, samples were withdrawn and subjected to immunoblot analysis. Strains LE670 (wild type)
864 and EC28 (Δ*bacA*) were included as controls. The position of BacA is indicated. **(B)** Morphological defects
865 induced by BacA depletion. Cells of strains LE670 (wild type) and EC41 (Δ*bacA* P_{Cu}-*bacA*) were grown in
866 medium containing 0.5 mM $CuSO_4$, washed, and incubated for 6 h in inducer-free medium before they
867 were transferred onto ASS-agarose pads lacking inducer and imaged at the indicated time points. Bar: 2
868 µm. **(C)** Changes in the growth pattern of *H. neptunium* in the absence of bactofilins. Cells of strains LE670
869 (wild type) and EC33 (Δ*bacAD*) were stained with the fluorescent D-amino acid HADA prior to analysis by
870 fluorescence microscopy. Shown are representative images of cells at different developmental stages.
871 Bars: 2 µm.

872 **Figure 2—figure supplement 1. Growth of Δ*bacAD* cells in a microfluidic flow cell.** Cells of strain EC33
873 (Δ*bacAD*) were flushed into a microfluidic flow cell and imaged at the indicated time points. Bar: 3 µm.

874 **Figure 2—figure supplement 2. Characterization of *H. neptunium* bactofilin mutants. (A)** Growth curves
875 *H. neptunium* strains LE670 (wild type), EC28 (Δ*bacA*), EC23 (Δ*bacD*) and EC33 (Δ*bacAD*). Exponentially
876 growing cultures were diluted into fresh media and monitored for 32 h using a microplate reader. Shown
877 are representative data from one out of three independent experiments. **(B)** Muropeptide profiles of
878 different *H. neptunium* strains. Cell walls of strains LE670 (wild type), EC28 (Δ*bacA*), EC23 (Δ*bacD*) and
879 EC33 (Δ*bacAD*) were digested with cellosyl to release muropeptides, which were reduced and separated
880 by HPLC. The identities of major muropeptide species, assigned based on the previously reported reten-
881 tion times (Cserti et al., 2017; Glauner, 1988), are given above the corresponding peaks. Tri, Tetra and
882 Penta stand for N-acetylglucosamine-N-acetylmuramitol tripeptide, tetrapeptide and pentapeptide,
883 respectively. "Anh" indicates muropeptides containing 1,6-anhydromuramic acid.

884 **Figure 3. BacA and BacD co-polymerize into filamentous structures. (A)** Model of a BacA trimer gener-
885 ated with AlphaFold-Multimer (Evans et al., 2022). Only residues P34-D138 are shown for each subunit.
886 **(B)** Visualization of BacA polymers. Purified BacA-His_6 was stained with uranyl acetate and imaged by
887 transmission electron microscopy (TEM). Arrowheads point to BacA filaments. Asterisks indicate filament
888 bundles and sheets. Bars: 200 nm. **(C)** Copolymerization of BacA and BacD after heterologous co-
889 expression in *E. coli*. Cells of *E. coli* BL21(DE3) transformed with plasmid pEC121 (P_{T7}-*bacA-eyfp* P_{T7}-*bacD-*
890 *ecfp*) were grown in LB medium containing 5 % glucose and induced with 0.5 mM IPTG prior to imaging.
891 Bar: 3 µm.

892 **Figure 4. BacA and BacD show a dynamic, cell cycle-dependent localization pattern. (A)** Localization
893 pattern of BacA-YFP. Cells of strain EC61 (*bacA*::*bacA-eyfp*) were transferred to agarose pads and imaged
894 at 20-min intervals. Shown are overlays of DIC and fluorescence images of a representative cell, with YFP
895 fluorescence shown in red. Scale bar: 3 µm. **(B)** Demographic analysis of BacA-YFP localization in swimmer
896 (left), stalked (middle), and budding (right) cells of strain EC61 (*bacA*::*bacA-eyfp*). The fluorescence inten-
897 sity profiles measured for cells of each type were sorted according to cell length and stacked on each
898 other, with the shortest cell shown at the top and the longest cell shown at the bottom (n=250 swimmer
899 cells, 215 stalked cells and 49 budding cells). Dotted red lines indicate the positions to which cells were
900 aligned. **(C)** Demographic analysis of BacD-Venus localization. Cells of strain EC67 (*bacD*::*bacD-venus*)
901 were analyzed as described in panel B (n=416 swimmer cells, 248 stalked cells and 45 budding cells). **(D)**
902 Co-localization of BacA and BacD in cells of strain EC68 (*bac*A::*bacA-eyfp bacD*::*bacD-mCherry*). Shown are
903 DIC images and overlays of the YFP and mCherry signals of representative cells, arranged according to
904 their developmental state. The individual signals are shown in **Figure S6A**. The Pearson's Correlation Coef-
905 ficient (PCC) of the two fluorescence signals in a random population of cells (n=454) is 0.506. Bar: 1 µm.

906 **Figure 4—figure supplement 1. Stability of the fluorescent protein fusions used in this study.** Cells of
907 strains LE670 (wild type), EC61 (*bacA*::*bacA-eyfp*), MO78 (*bacA*::*bacA*$_{F130R}$*-eyfp*) and EC67 (*bacD*::*bacD-*
908 *venus*) were subjected to immunoblot analysis using anti-GFP antibodies.

909 **Figure 4—figure supplement 2. Localization dynamics of BacA-YFP.** Cells of strain EC61 (*bacA*::*bacA-eyfp*)
910 were flushed into a microfluidic flow cell and imaged at 15-min intervals over multiple cell cycles. Shown
911 are overlays of DIC and fluorescence images. Bar: 2 µm.

912 **Figure 4—figure supplement 3. Dependence of BacD localization on BacA. (A)** Co-localization of BacA
913 and BacD in cells of strain EC68 (*bac*A::*bacA-eyfp bacD*::*bacD-mCherry*). Shown are the individual fluor-
914 escence images used to generate the overlays in **Figure 4D**. **(B)** Random localization of BacD complexes in
915 the absence of BacA. Cells of strain EC60 (Δ*bacA* P_{Zn}::P_{Zn}-*bacD-venus*) were grown in inducer-free medium
916 and induced for 4 h with 0.5 mM $ZnSO_4$ prior to imaging. Bar: 3 µm.

917 **Figure 4—figure supplement 4. Localization and functionality of BacA$_{F130R}$-YFP.** Cells of strain MO78
918 (*bacA*::*bacA*$_{F130R}$*-eyfp*), producing the polymerization-deficient BacA$_{F130R}$-YFP variant instead of the native
919 protein, were grown to exponential phase and imaged. Bar: 3 µm.

920 **Figure 5. The single-particle dynamics of BacA change over the course of the cell cycle. (A)** Representa-
921 tive heat maps showing the sum of single-particle positions observed in live-cell single-particle localization
922 microscopy studies of a swimmer, stalked and budding cell producing BacA-YFP (EC61) or a mutant cell

923 producing the polymerization-deficient $BacA_{F130R}$-YFP variant (MO78). Insets show the corresponding
924 bright-field images. Bars: 1 µm. **(B)** Mean-squared displacement (MSD) analysis of the mobility of BacA-
925 YFP in wild-type swimmer (n=100), stalked (n=105) and budding (n=101) cells (EC61). Cells (n=110) produc-
926 ing the $BacA_{F130R}$-YFP were analyzed as a control (MO78). Error bars indicate the standard deviation. **(C)**
927 Bubble plots showing the proportions of mobile and immobile particles (size of the bubbles) and the cor-
928 responding average diffusion constants (y-axis) in the cells analyzed in panel B.

929 **Figure 5—figure supplement 1. Single-particle tracking analysis of BacA-YFP mobility.** Shown is a
930 Gaussian mixture model (GMM) analysis of the mobility of the BacA-YFP variants analyzed in **Figure 3B**.
931 The distributions of the frame-to-frame displacements in both x and y direction from single-particle
932 tracking experiments were fitted to a two-component Gaussian function (sum in black), assuming a fast-
933 diffusing mobile (dotted blue lines) and a slow-diffusing (dotted red lines) population.

934 **Figure 6. Putative operons comprising adjacent BacA and M23 peptidase genes are widely conserved**
935 **among bacteria. (A)** Arrangement of *bacA* and *lmdC* genes in species whose BacA homolog has a proven
936 role in cell morphogenesis. **(B)** Co-conservation of BacA and M23 peptidase genes across different bacte-
937 rial phyla. Bioinformatic analysis was used to identified genomes that contained a bactofilin gene located
938 next to an M23 peptidase gene. After retrieval of the taxonomy IDs of the corresponding species from the
939 National Center for Biotechnology Information (NCBI) website, a phylogenetic tree of the species was
940 created using the iTOL server (Letunic and Bork, 2021). Abbreviations: DT (Deinococcus-Thermus group),
941 FCB (Fibrobacteres-Chlorobi-Bacteroidetes group), β (β-proteobacteria), δ (δ-proteobacteria). The full list
942 of species used and details on the genes identified are provided in Dataset 2.

943 **Figure 7. LmdC is a peptidoglycan hydrolase with DD-endopeptidase activity. (A)** Predicted domain archi-
944 tecture of *H. neptunium* LmdC. The predicted positions of the transmembrane helix (TM), the three coiled-
945 coil regions (CC) and the M23 peptidase domain are indicated. **(B)** Alignment of the amino acid sequences
946 of multiple M23 peptidases showing the conservation of the catalytic residues in LmdC. Residues required
947 to coordinate the catalytic Zn^{2+} ion of LytM from *S. aureus* (Firczuk et al., 2005) are indicated by arrow-
948 heads. The proteins shown are EnvC from *E. coli* (UniProt: P37690), NlpD from *E. coli* (P0ADA3), LytM from
949 *S. aureus* (O33599), MepM from *E. coli* (P0AFS9) and LmdC from *H. neptunium* (Q0BYX6). **(C)** Predicted
950 molecular structure of *H. neptunium* LmdC, generated with Alphafold2 (Jumper et al., 2021). The different
951 domains of the protein and the position of proline 66, which terminates the N-terminal fragment of LmdC
952 used for the *in vivo* analyses in this study ($LmdC_{1-66}$) are indicated. **(D)** HPLC traces showing the muro-
953 peptide profile of peptidoglycan treated with LmdC. Cell walls were incubated with the isolated M23 pep-

954 tidase domain of LmdC at pH 5.0 and pH 7.5. Subsequently, muropeptides were released with cellosyl,
955 reduced and separated by HPLC. A control sample lacked LmdC (No protein). The nature of the major
956 products is indicated above the peaks. Tri, Tetra and Penta stand for N-acetylglucosamine-N-acetylmura-
957 mitol tripeptide, tetrapeptide and pentapeptide, respectively. **(E)** Structure of a TetraTetra muropeptide.
958 Abbreviations: G (N-acetylglucosamine), M (N-acetylmuramic acid). The cleavage site of LmdC is indicated
959 by a red arrowhead.

960 **Figure 8. LmdC colocalizes and directly interacts with BacA. (A)** Domain architectures of the native LmdC
961 protein and the $LmdC_{1-66}$-mCherry fusion used for co-localization studies. The transmembrane helix is
962 shown in purple. Abbreviations: CC (coiled-coil domain), M23 (M23 peptidase domain), CHY (mCherry).
963 **(B)** Co-localization of BacA-YFP and $LmdC^N$-mCherry in *H. neptunium*. Shown are representative cells of
964 strain MO79 (*bacA*::*bacA-eyfp* P_{Cu}::P_{Cu}-*lmdC*^{N}-*mCherry* that were induced for 2 h with 0.5 mM $CuSO_4$ prior
965 to analysis by DIC and fluorescence microscopy. **(C)** Demographic analysis of BacA-YFP and $LmdC^N$-
966 mCherry co-localization in swimmer (left; n=99), stalked (middle; n=103) and budding (right; n=22) cells
967 from the culture imaged in panel B. Data were analyzed as described for **Figure 4B**. Corresponding fluor-
968 escence profiles are shown at the same relative position in the two graphs. **(D)** Bio-layer interferometric
969 analysis of the interaction between cytoplasmic domain of LmdC and BacA. Sensors derivatized with a
970 biotinylated synthetic peptide comprising the N-terminal cytoplasmic region of LmdC (amino acids 1-38)
971 were probed with the indicated concentrations of BacA. After the association of BacA, the sensors were
972 transferred to protein-free buffer to induce BacA dissociation. The interaction kinetics were followed by
973 monitoring the wavelength shifts resulting from changes in the optical thickness of the sensor surface
974 during association or dissociation of the analyte. The extent of non-specific binding of BacA to the sensor
975 surface was negligible (control). **(E)** Affinity of the BacA-LmdC interaction. The maximal wavelength shifts
976 measured in the experiment shown in panel D were plotted against the corresponding BacA concentra-
977 tion. The data were fitted to a one-site binding model, yielding an apparent K_d value of ~15 µM.

978 **Figure 8—figure supplement 1. Random localization of $LmdC_{1-66}$-mCherry in the Δ*bacAD* background.**
979 Cells of strain MO80 (Δ*bacAD* P_{Cu}::P_{Cu}-*lmdC*$_{1-66}$-*mCherry*) were induced for 2 h with 0.5 mM $CuSO_4$ prior to
980 imaging. mCherry fluorescence is shown in yellow. Bar: 3 µm.

981 **Figure 9. BacA and LmdC contribute to cell morphogenesis in *R. rubrum*. (A)** Schematic representation
982 of the *bacA-lmdC* operon in *R. rubrum*. **(B)** Domain organization of BacA from *R. rubrum*. The bactofilin
983 polymerization domain (green box) is flanked by non-structured N- and C-terminal regions. **(C)** Phenotypes
984 of *R. rubrum* wild-type (S1), Δ$bacA_{Rs}$ (SP70), Δ$lmdC_{Rs}$ (SP68) and Δ$bacA_{Rs}$ Δ$lmdC_{Rs}$ (SP116) cells, imaged

985 using phase-contrast microscopy. Bar: 5 µm. **(D)** Superplots showing the distribution of cell sinuosities in
986 populations of the indicated *R. rubrum* strains. Small dots represent the data points, large dots represent
987 the median values of the three independent experiments shown in the graphs (dark blue, light blue, grey).
988 The mean of the three median values is indicated by a horizontal red line. Whiskers represent the standard
989 deviation. *** p<0.005; ns, not significant; t-test). **(E)** Co-localization of $BacA_{Rs}$-mCherry and $LmdC^{N}_{Rs}$-
990 mNeonGreen in the Δ$lmdC_{Rs}$ background (SP119). The Pearson's Correlation Coefficient (PCC) of the two
991 fluorescence signals in a random subpopulation of cells (n=87) is 0.515. Scale bar: 5 µm. **(F)** Localization
992 of $BacA_{Rs}$-mNeonGreen in the Δ$lmdC_{Rs}$ background (SP98). Bar: 5 µm. **(G)** Localization of $LmdC_{Rs}$-mNeon-
993 Green in the Δ$bacA_{Rs}$ background (SP118). Bar: 5 µm.

994 **Figure 9—figure supplement 1. Analysis of BacA and LmdC from *R. rubrum*. (A)** Clearer visualization of
995 the abnormal curvature of BacA- and LmdC-deficient *R. rubrum* cells by inhibition of cell division. Cells of
996 strains SP68 (Δ*lmdC*), SP70 (Δ*bacA*) and SP116 (Δ*lmdC* Δ*bacA*) were treated with 5 µg/ml cefalexin (Cfx)
997 for 6 h. Bar: 5 µm. **(B)** Muropeptide profiles of different *R. rubrum* strains. Cell walls of strains S1 (wild
998 type), SP70 (Δ$bacA_{Rs}$) and SP68 (Δ*lmdC*) were digested with cellosyl to release muropeptides, which were
999 reduced and separated by HPLC chromatography. The identities of major muropeptide species, assigned
1000 based on the previously reported retention times (Glauner, 1988), are given above the corresponding
1001 peaks. Tetra stands for N-acetylglucosamine-N-acetylmuramitol tetrapeptide. "Anh" indicates muropep-
1002 tides containing 1,6-anhydromuramic acid.

1003 **Figure 9—figure supplement 2. Cell lengths of *R. rubrum* strains.** Superplots showing the distribution of
1004 cell sinuosities in populations of strains S1 (wild type), SP105 (Δ$bacA_{Rs}$ P_{bacA}-$bacA_{Rs}$) and SP109
1005 ($bacA_{Rs}$::$bacA_{Rs}$-*mCherry*). Small dots represent the data points, large dots represent the median values of
1006 the three independent experiments shown in the graphs (dark blue, light blue, grey). The mean of the
1007 three median values is indicated by a horizontal line. Whiskers represent the standard deviation. ***
1008 p<0.005; ns, not significant; t-test).

1009 **Figure 9—figure supplement 3. Lysis of *E. coli* upon heterologous expression of full-length *R. rubrum***
1010 ***lmdC*.** Shown are cells of *E. coli* Rosetta(DE3)pLysS harboring pSP120 (P_{T7}-$lmdC_{Rs}$) or the corresponding
1011 empty vector imaged 4h after the induction of gene expression with 0.5 mM IPTG. Arrowheads indicate
1012 ghost cells, cell debris, lysing cells or strongly elongated cells. Scale bar: 5 µm.

1013 **Figure 9—figure supplement 4. Analysis of *R. rubrum* strains producing fluorescent protein fusions. (A)**
1014 Levels of the $LmdC^{N}_{Rs}$-mNeonGreen fusion in different *R. rubrum* strains. Strains SP98 (Δ$lmdC_{Rs}$
1015 $bacA_{Rs}$::$bacA_{Rs}$-*mNeongreen*), SP114 ($bacA_{Rs}$::$bacA_{Rs}$-*mCherry* P_{lmdC}-$lmdC^{N}_{Rs}$-*mNeongreen*), SP118 (Δ*bacA*

1016 Δ*lmdC* P_{lmdC}-*lmdC*$_{1-80}$-*mNeongreen*) and SP119 (*bacA*::*bacA-mCherry* Δ*lmdC* P_{lmdC}-*lmdC*$_{1-80}$-*mNeongreen*)
1017 were subjected to immunoblot analysis with an anti-mNeonGreen antibody. Predicted molecular weights:
1018 BacA$_{Rs}$-mNeonGreen (44.8 kDa), LmdC$^{N}_{Rs}$-mNeonGreen fusion (35.9 kDa) **(B)** Levels of the BacA$_{Rs}$-mCherry
1019 fusion in different *R. rubrum* strains. Strains SP109 (*bacA*$_{Rs}$::*bacA*$_{Rs}$-*mCherry*), SP114 (*bacA*$_{Rs}$::*bacA*$_{Rs}$-
1020 *mCherry* P_{lmdC}-*lmdC*$^{N}_{Rs}$-*mNeongreen*), SP117 (*bacA*$_{Rs}$::*bacA*$_{Rs}$-*mCherry* Δ*lmdC*) and SP119 (*bacA*$_{Rs}$::*bacA*$_{Rs}$-
1021 *mCherry* Δ*lmdC* P_{lmdC}-*lmdC*$^{N}_{Rs}$-*mNeongreen*) were subjected to immunoblot analysis with an anti-mCherry
1022 antibody. The predicted molecular weight of BacA$_{Rs}$-mCherry is 44.9 kD. **(C)** Co-localization of BacA$_{Rs}$-
1023 mCherry and LmdC$_{Rs}$-mNeongreen in *R. rubrum* cells carrying the native *lmdC*$_{Rs}$ gene. The Pearson's
1024 Correlation Coefficient (PCC) of the two fluorescence signals in a random subpopulation of cells (n=177)
1025 is 0.54. Scale bar: 5 µm.

1026 **Figure 10. Model of the roles of BacA and LmdC in *H. neptunium* and *R. rubrum* cell morphogenesis. (A)**
1027 Cell morphogenesis in *H. neptunium* wild-type (top) and Δ*bacAD* cells (bottom). In wild-type cells, BacA
1028 polymers form a complex with the DD-endopeptidase LmdC at the future stalked pole. The hydrolytic
1029 activity of LmdC helps to curve the cell wall at the incipient stalk base and thus determine stalk mor-
1030 phology. The zone of high positive inner cell curvature, and potentially the physical barrier constituted by
1031 the bactofilin polymer, prevent the movement of elongasome complexes from the mother cell body into
1032 the stalk, thereby limiting peptidoglycan biosynthesis to the stalked cell pole. At a later stage, the bacto-
1033 filin-LmdC complex localizes close to the tip of the stalk and again generates a ring-shaped zone of positive
1034 cell curvature, thereby promoting the remodeling of the stalk tip into a spherical bud. At the onset of the
1035 budding process, elongasome complexes accumulate in the nascent bud by a so-far unknown mechanism.
1036 The positively curved bud neck and the bactofilin polymers prevent the movement of elongasome com-
1037 plexes from the bud into the stalk, thereby limiting cell growth to the bud compartment. In the Δ*bacAD*
1038 mutant, cells fail to concentrate LmdC at the future stalk base and bud neck. As a consequence, peptido-
1039 glycan biosynthesis is no longer limited to the different growth zones, leading to pseudo-stalk formation
1040 and unregulated bud expansion. **(B)** Bactofilin-mediated modulation of cell helicity in *R. rubrum*. BacA$_{Rs}$
1041 (yellow) recruits LmdC$_{Rs}$ (red) to the inner cell curvature. The hydrolytic activity of LmdC ultimately stimu-
1042 lates peptidoglycan biosynthesis at this position, leading to a reduction in cell helicity.

Video legends

1043 **Video 1. Unregulated growth of a bactofilin-deficient *H. neptunium* mutant.** Cells of strain EC33
1044 (Δ*badAD*) were grown in a microfluidic flow cell and imaged by DIC microsopy at 15 min intervals. Bar:
1045 2 µm.

1046 **Video 2. Normal growth of the *H. neptunium* wild-type strain.** Cells of strain LE670 (wild type) were
1047 grown in a microfluidic flow cell and imaged by DIC microscopy at 5 min intervals. Bar: 2 µm.

1048 **Videos 3. Localization dynamics of BacA-YFP (example 1).** Cells of strain EC61 (*bacA::bacA-eyfp*) were
1049 grown in a microfluidic flow cell and imaged at 15 min intervals. Shown are overlays of DIC and
1050 fluorescence images. YFP fluorescence is shown in red for better visibility. Bar: 2 µm.

1051 **Videos 4. Localization dynamics of BacA-YFP (example 2).** Images were taken as described for Video 3.
1052 Bar: 2 µm.

1053 **Videos 5. Localization dynamics of BacA-YFP (example 3).** Images were taken as described for Video 3.
1054 Bar: 2 µm.

Figures

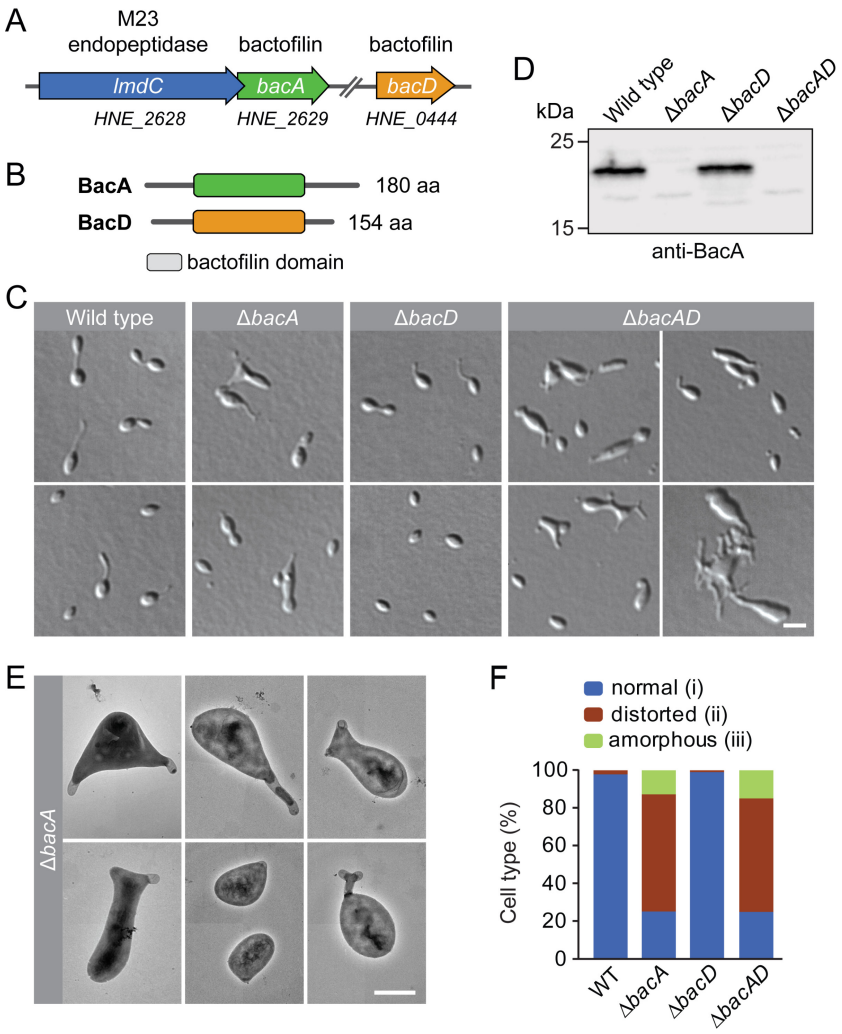

Figure 1. Bactofilin BacA is required for proper cell morphology in *H. neptunium*. (A) Schematic representation of the two bactofilin genes present in the *H. neptunium* genome. *bacA* lies adjacent to the M23 peptidase gene *lmdC*. Arrows indicate the direction of transcription. **(B)** Domain organization of BacA and BacD from *H. neptunium*. The bactofilin polymerization domain (colored boxes) is flanked by non-structured N- and C-terminal regions. **(C)** Morphology of *H. neptunium* bactofilin mutants. Shown are representative cells of strains LE670 (wild type), EC28 (Δ*bacA*), EC23 (Δ*bacD*) and EC33 (Δ*bacAD*), imaged by differential interference contrast (DIC) microscopy. Bar: 4 µm. **(D)** Immunoblot analysis of the strains shown in panel C, performed using anti-BacA antibodies. **(E)** Transmission electron micrographs of Δ*bacA* cells at the early stalked-cell stage. Bar: 1 µm. **(F)** Quantification of the proportion of phenotypically abnormal stalked and budding cells in cultures of the strains analyzed in panel C (n = 100 cells per strain).

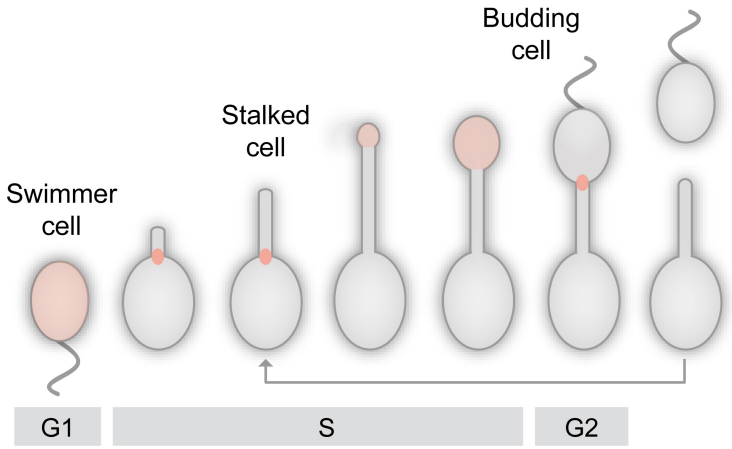

1064 **Figure 1—figure supplement 1. The dimorphic lifecycle of *H. neptunium*.** A motile, flagellated swimmer sheds its flagellum and
1065 forms a stalk at the opposite cell pole. A a defined point in the cell cycle, the terminal segment of the stalk dilates and develops
1066 into a new swimmer cell. After cell division, the newborn swimmer cell first needs to differentiate into a stalked cell to initiate a
1067 new round of cell division, whereas the stalked mother cell immediately enters the next replication cycle. The predominant
1068 growth zones (Cserti et al., 2017) are indicated in red.

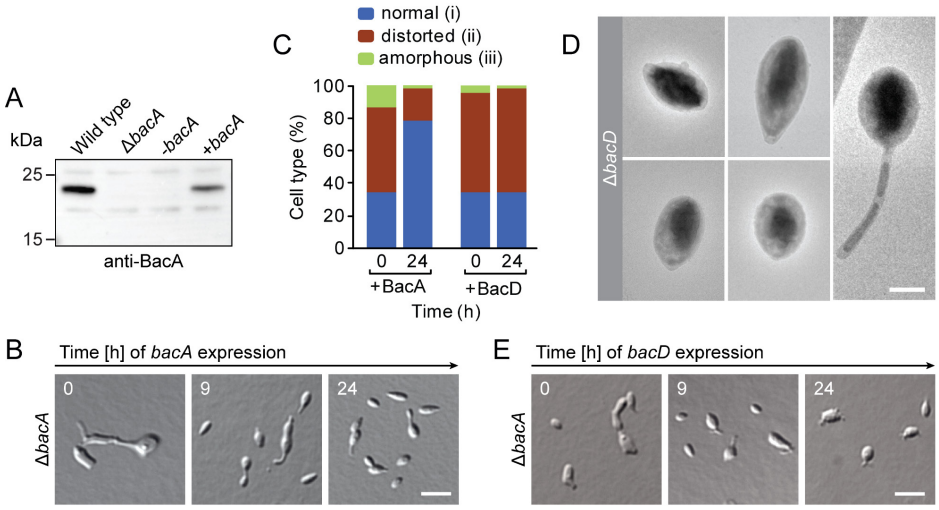

1069 **Figure 1—figure supplement 2. Phenotypic analysis of *H. neptunium* bactofilin mutants. (A)** Immunoblot analysis of strains
1070 LE670 (wild type), EC28 (Δ*bacA*) and EC41 (Δ*bacA* P_{Cu}::P_{Cu}-*bacA*) grown in the absence (-*bacA*) and presence (+*bacA*) of 0.5 mM
1071 $CuSO_4$, performed with an anti-BacA antibody. **(B)** Rescue of the phenotype of a Δ*bacA* mutant by ectopic expression of *bacA*.
1072 Cells of strain EC41 (Δ*bacA* P_{Cu}::P_{Cu}-*bacA*) were grown in copper-free medium, induced by the addition of copper, and imaged
1073 after the indicated time incubation times. Bar: 3 µm. **(C)** Quantification of the proportion of phenotypically abnormal stalked and
1074 budding cells in the cultures of strains EC41 (Δ*bacA* P_{Cu}::P_{Cu}-*bacA*) and EC43 (Δ*bacA* P_{Zn}::P_{Zn}-*bacD*) analyzed in panels B and E
1075 before (t=0 h) and 24 h after induction (n = 100 cells per time point). **(D)** Transmission electron micrographs of Δ*bacD* cells at the
1076 swimmer and stalk cell stage. Bar: 1 µm. **(E)** DIC images of a Δ*bacA* mutant overproducing BacD from a zinc-inducible promoter.
1077 Cells of strain EC43 (Δ*bacA* P_{Zn}::P_{Zn}-*bacD*) were grown in inducer-free medium, induced by the addition of 0.5 mM $ZnSO_4$, and
1078 imaged after the indicated incubation times. Bar: 3 µm.

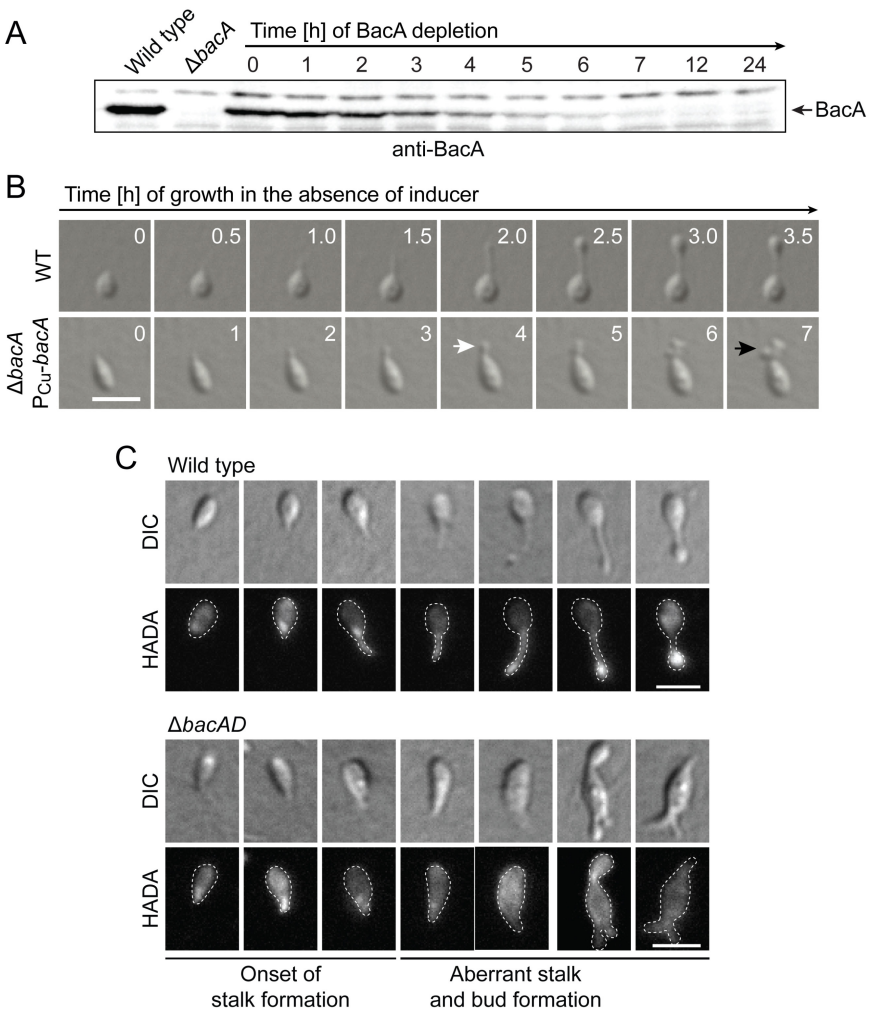

1079 **Figure 2. Lack of BacA leads to uncontrolled growth of the stalk and bud compartments. (A)** Immunoblot showing the levels of
1080 BacA in strain EC41 (Δ*bacA* P_{Cu}-*bacA*) over the course of BacA depletion. Cells were grown in copper-containing medium, washed
1081 and transferred to inducer-free medium. At the indicated time points, samples were withdrawn and subjected to immunoblot
1082 analysis. Strains LE670 (wild type) and EC28 (Δ*bacA*) were included as controls. The position of BacA is indicated. **(B)**
1083 Morphological defects induced by BacA depletion. Cells of strains LE670 (wild type) and EC41 (Δ*bacA* P_{Cu}-*bacA*) were grown in
1084 medium containing 0.5 mM $CuSO_4$, washed, and incubated for 6 h in inducer-free medium before they were transferred onto
1085 ASS-agarose pads lacking inducer and imaged at the indicated time points. Bar: 2 µm. **(C)** Changes in the growth pattern of
1086 *H. neptunium* in the absence of bactofilins. Cells of strains LE670 (wild type) and EC33 (Δ*bacAD*) were stained with the fluorescent
1087 D-amino acid HADA prior to analysis by fluorescence microscopy. Shown are representative images of cells at different
1088 developmental stages. Bars: 2 µm.

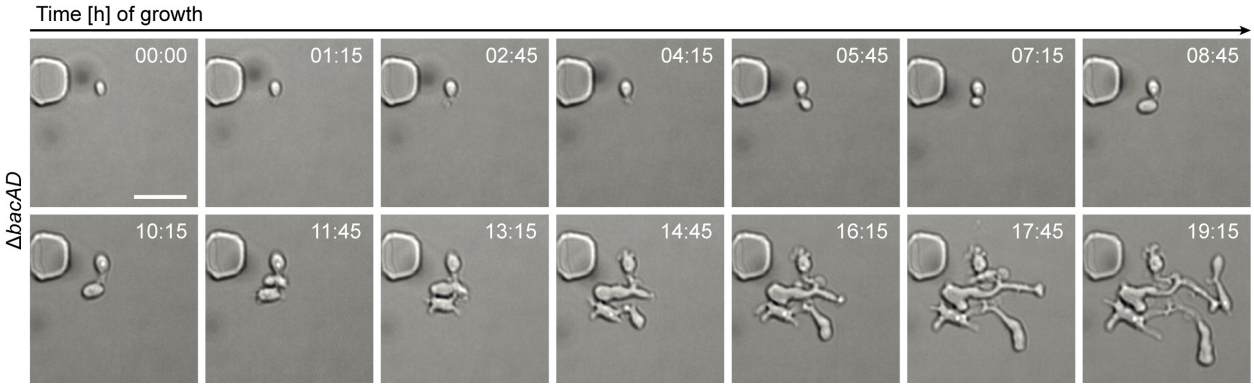

1089 **Figure 2—figure supplement 1. Growth of Δ*bacAD* cells in a microfluidic flow cell.** Cells of strain EC33 (Δ*bacAD*) were flushed
1090 into a microfluidic flow cell and imaged at the indicated time points. Bar: 3 µm.

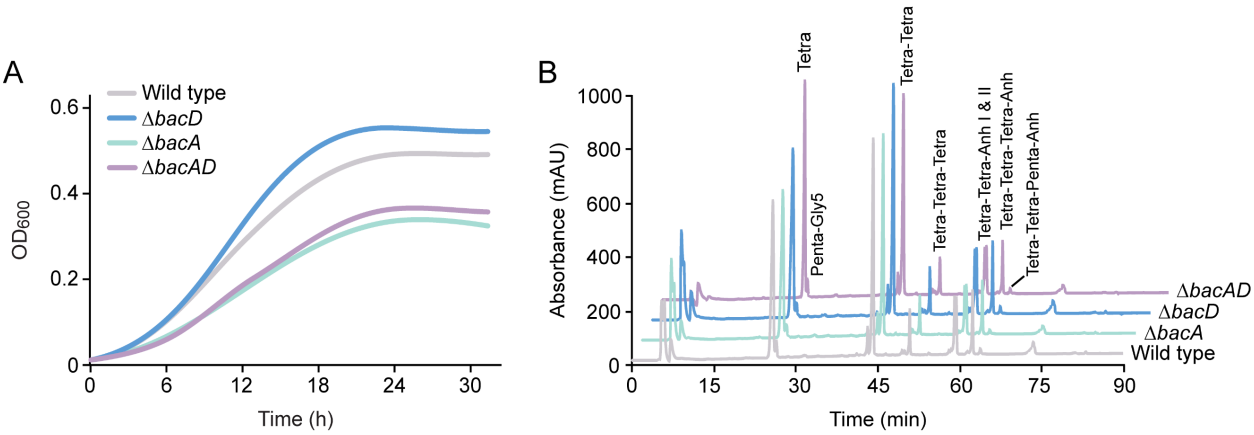

1091 **Figure 2—figure supplement 2. Characterization of *H. neptunium* bactofilin mutants. (A)** Growth curves *H. neptunium* strains
1092 LE670 (wild type), EC28 (Δ*bacA*), EC23 (Δ*bacD*) and EC33 (Δ*bacAD*). Exponentially growing cultures were diluted into fresh media
1093 and monitored for 32 h using a microplate reader. Shown are representative data from one out of three independent
1094 experiments. **(B)** Muropeptide profiles of different *H. neptunium* strains. Cell walls of strains LE670 (wild type), EC28 (Δ*bacA*),
1095 EC23 (Δ*bacD*) and EC33 (Δ*bacAD*) were digested with cellosyl to release muropeptides, which were reduced and separated by
1096 HPLC. The identities of major muropeptide species, assigned based on the previously reported retention times (Cserti et al., 2017;
1097 Glauner, 1988), are given above the corresponding peaks. Tri, Tetra and Penta stand for N-acetylglucosamine-N-acetylmuramitol
1098 tripeptide, tetrapeptide and pentapeptide, respectively. “Anh” indicates muropeptides containing 1,6-anhydromuramic acid.

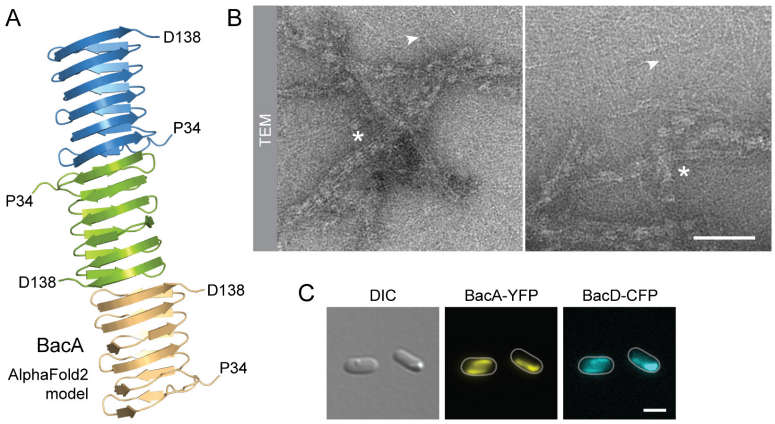

1099 **Figure 3. BacA and BacD co-polymerize into filamentous structures. (A)** Model of a BacA trimer generated with AlphaFold-
1100 Multimer (Evans et al., 2022). Only residues P34-D138 are shown for each subunit. **(B)** Visualization of BacA polymers. Purified
1101 BacA-His_6 was stained with uranyl acetate and imaged by transmission electron microscopy (TEM). Arrowheads point to BacA
1102 filaments. Asterisks indicate filament bundles and sheets. Bars: 200 nm. **(C)** Copolymerization of BacA and BacD after
1103 heterologous co-expression in *E. coli*. Cells of *E. coli* BL21(DE3) transformed with plasmid pEC121 (P_{T7}-*bacA-eyfp* P_{T7}-*bacD-ecfp*)
1104 were grown in LB medium containing 5 % glucose and induced with 0.5 mM IPTG prior to imaging. Bar: 3 µm.

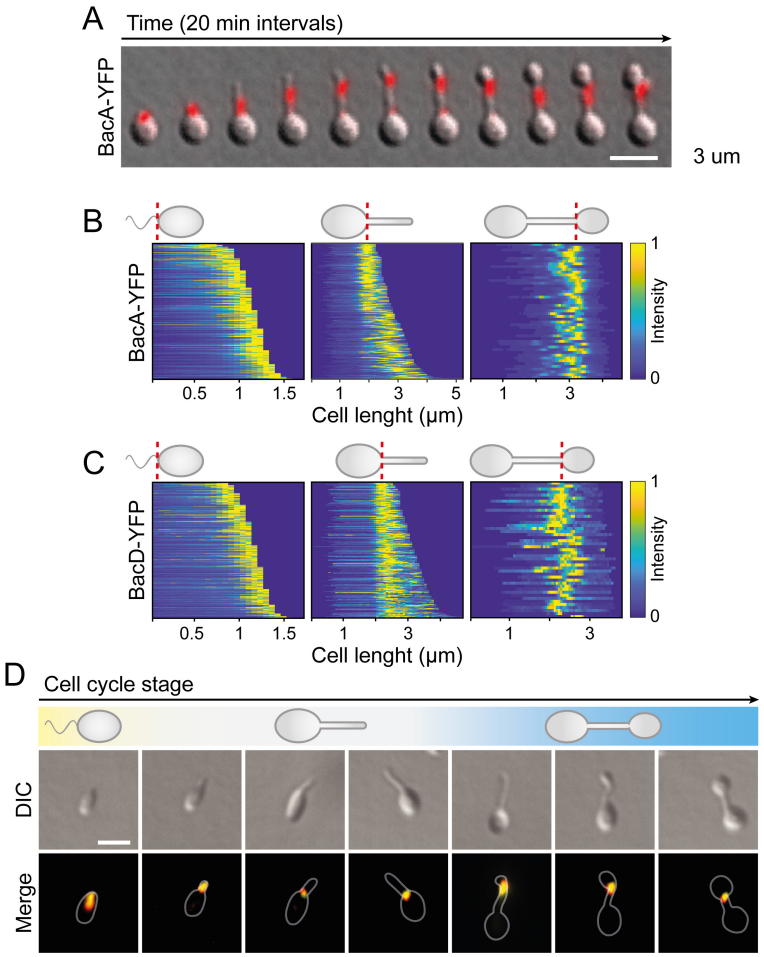

Figure 4. BacA and BacD show a dynamic, cell cycle-dependent localization pattern. (A) Localization pattern of BacA-YFP. Cells of strain EC61 (*bacA*::*bacA-eyfp*) were transferred to agarose pads and imaged at 20-min intervals. Shown are overlays of DIC and fluorescence images of a representative cell, with YFP fluorescence shown in red. Scale bar: 3 µm. **(B)** Demographic analysis of BacA-YFP localization in swimmer (left), stalked (middle), and budding (right) cells of strain EC61 (*bacA*::*bacA-eyfp*). The fluorescence intensity profiles measured for cells of each type were sorted according to cell length and stacked on each other, with the shortest cell shown at the top and the longest cell shown at the bottom (n=250 swimmer cells, 215 stalked cells and 49 budding cells). Dotted red lines indicate the positions to which cells were aligned. **(C)** Demographic analysis of BacD-Venus localization. Cells of strain EC67 (*bacD*::*bacD-venus*) were analyzed as described in panel B (n=416 swimmer cells, 248 stalked cells and 45 budding cells). **(D)** Co-localization of BacA and BacD in cells of strain EC68 (*bac*A::*bacA-eyfp bacD*::*bacD-mCherry*). Shown are DIC images and overlays of the YFP and mCherry signals of representative cells, arranged according to their developmental state. The individual signals are shown in **Figure S6A**. The Pearson's Correlation Coefficient (PCC) of the two fluorescence signals in a random population of cells (n=454) is 0.506. Bar: 1 µm.

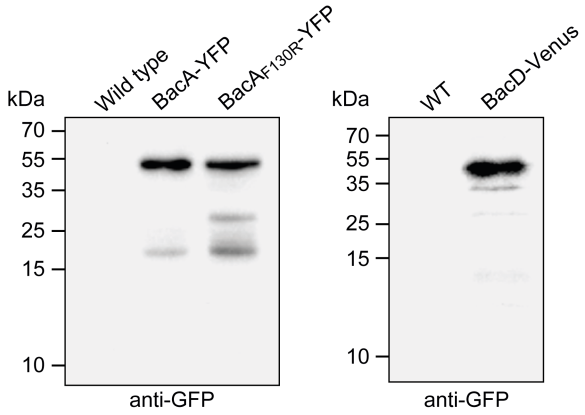

1117 **Figure 4—figure supplement 1. Stability of the fluorescent protein fusions used in this study.** Cells of strains LE670 (wild type),
1118 EC61 (*bacA*::*bacA-eyfp*), MO78 (*bacA*::*bacA*$_{F130R}$*-eyfp*) and EC67 (*bacD*::*bacD-venus*) were subjected to immunoblot analysis using
1119 anti-GFP antibodies.

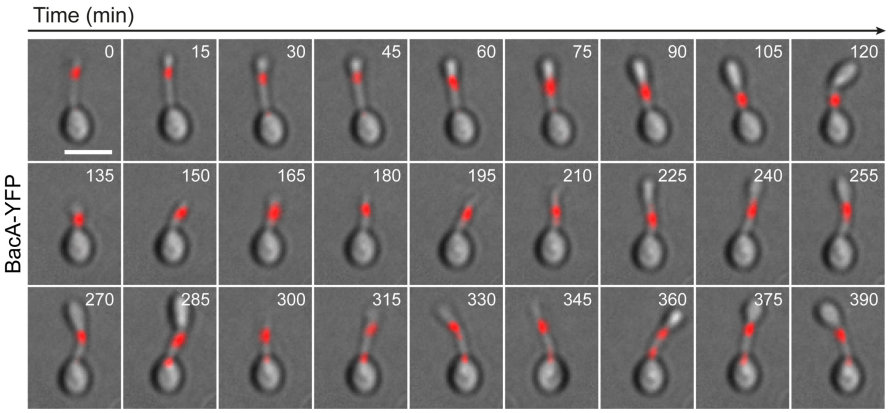

1120 **Figure 4—figure supplement 2. Localization dynamics of BacA-YFP.** Cells of strain EC61 (*bacA*::*bacA-eyfp*) were flushed into a
1121 microfluidic flow cell and imaged at 15-min intervals over multiple cell cycles. Shown are overlays of DIC and fluorescence images.
1122 Bar: 2 µm.

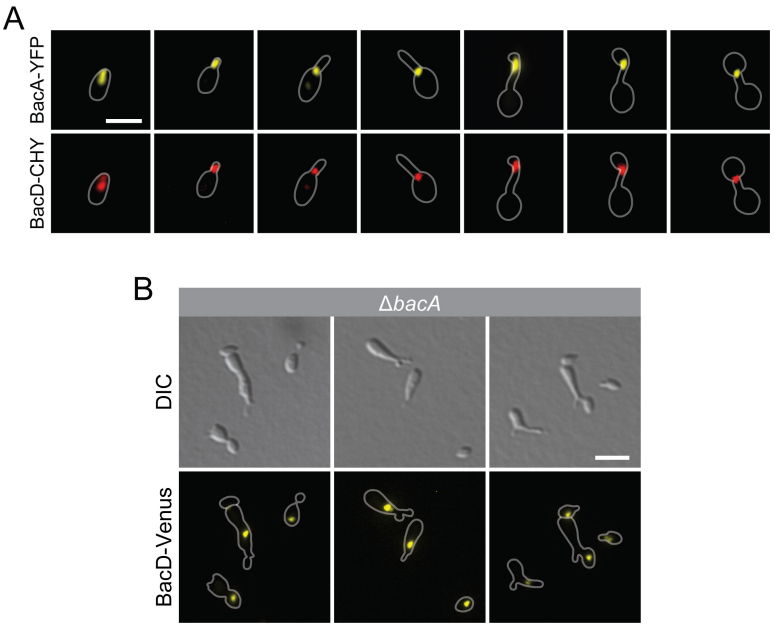

1123 **Figure 4—figure supplement 3. Dependence of BacD localization on BacA. (A)** Co-localization of BacA and BacD in cells of strain
1124 EC68 (*bac*A::*bacA-eyfp bacD*::*bacD-mCherry*). Shown are the individual fluorescence images used to generate the overlays in
1125 **Figure 4D**. **(B)** Random localization of BacD complexes in the absence of BacA. Cells of strain EC60 (Δ*bacA* P_{Zn}::P_{Zn}-*bacD-venus*)
1126 were grown in inducer-free medium and induced for 4 h with 0.5 mM $ZnSO_4$ prior to imaging. Bar: 3 µm.

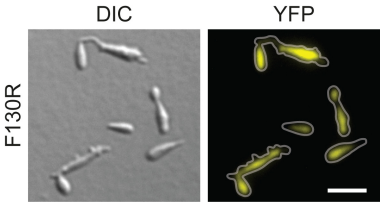

1127 **Figure 4—figure supplement 4. Localization and functionality of $BacA_{F130R}$-YFP.** Cells of strain MO78 (*bacA*::*$bacA_{F130R}$-eyfp*),
1128 producing the polymerization-deficient $BacA_{F130R}$-YFP variant instead of the native protein, were grown to exponential phase and
1129 imaged. Bar: 3 µm.

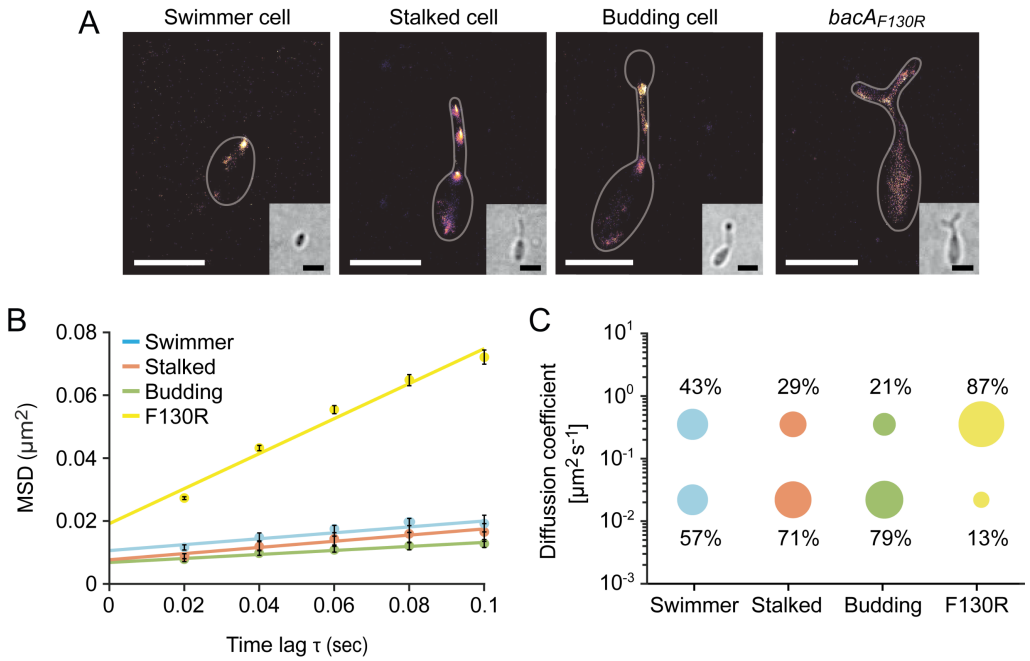

Figure 5. The single-particle dynamics of BacA change over the course of the cell cycle. (A) Representative heat maps showing the sum of single-particle positions observed in live-cell single-particle localization microscopy studies of a swimmer, stalked and budding cell producing BacA-YFP (EC61) or a mutant cell producing the polymerization-deficient $BacA_{F130R}$-YFP variant (MO78). Insets show the corresponding bright-field images. Bars: 1 µm. **(B)** Mean-squared displacement (MSD) analysis of the mobility of BacA-YFP in wild-type swimmer (n=100), stalked (n=105) and budding (n=101) cells (EC61). Cells (n=110) producing the $BacA_{F130R}$-YFP were analyzed as a control (MO78). Error bars indicate the standard deviation. **(C)** Bubble plots showing the proportions of mobile and immobile particles (size of the bubbles) and the corresponding average diffusion constants (y-axis) in the cells analyzed in panel B.

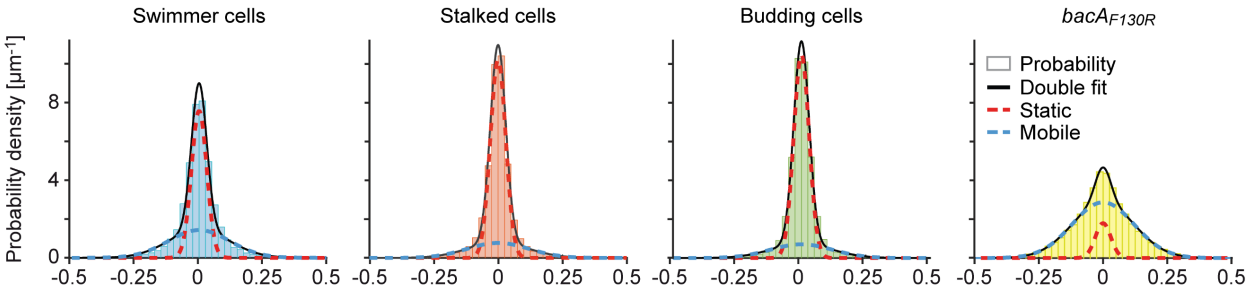

Figure 5—figure supplement 1. Single-particle tracking analysis of BacA-YFP mobility. Shown is a Gaussian mixture model (GMM) analysis of the mobility of the BacA-YFP variants analyzed in **Figure 3B**. The distributions of the frame-to-frame displacements in both x and y direction from single-particle tracking experiments were fitted to a two-component Gaussian function (sum in black), assuming a fast-diffusing mobile (dotted blue lines) and a slow-diffusing (dotted red lines) population.

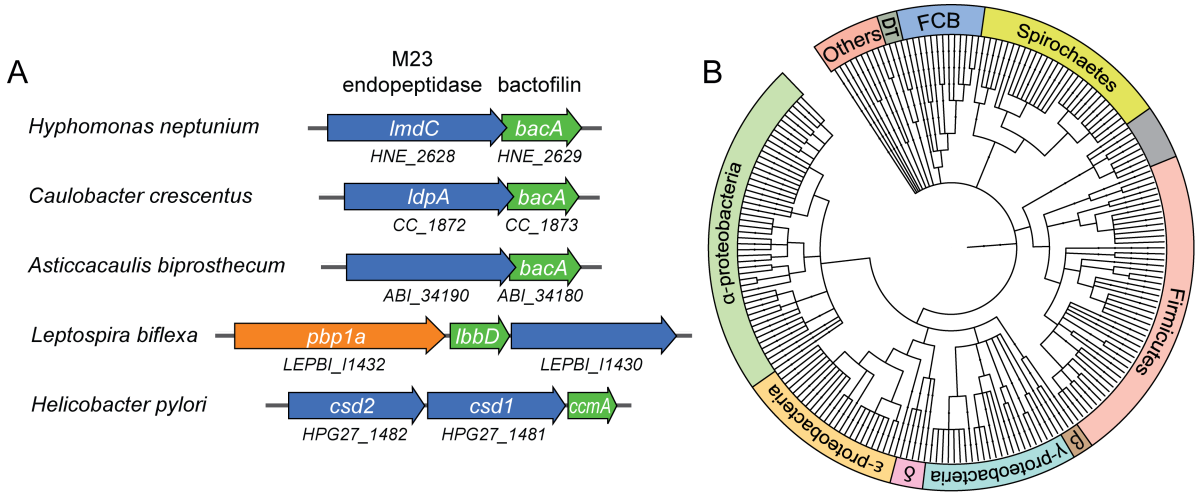

Figure 6. Putative operons comprising adjacent BacA and M23 peptidase genes are widely conserved among bacteria. (A) Arrangement of *bacA* and *lmdC* genes in species whose BacA homolog has a proven role in cell morphogenesis. **(B)** Co-conservation of BacA and M23 peptidase genes across different bacterial phyla. Bioinformatic analysis was used to identified genomes that contained a bactofilin gene located next to an M23 peptidase gene. After retrieval of the taxonomy IDs of the corresponding species from the National Center for Biotechnology Information (NCBI) website, a phylogenetic tree of the species was created using the iTOL server (Letunic and Bork, 2021). Abbreviations: DT (Deinococcus-Thermus group), FCB (Fibrobacteres-Chlorobi-Bacteroidetes group), β (β-proteobacteria), δ (δ-proteobacteria). The full list of species used and details on the genes identified are provided in Dataset 2.

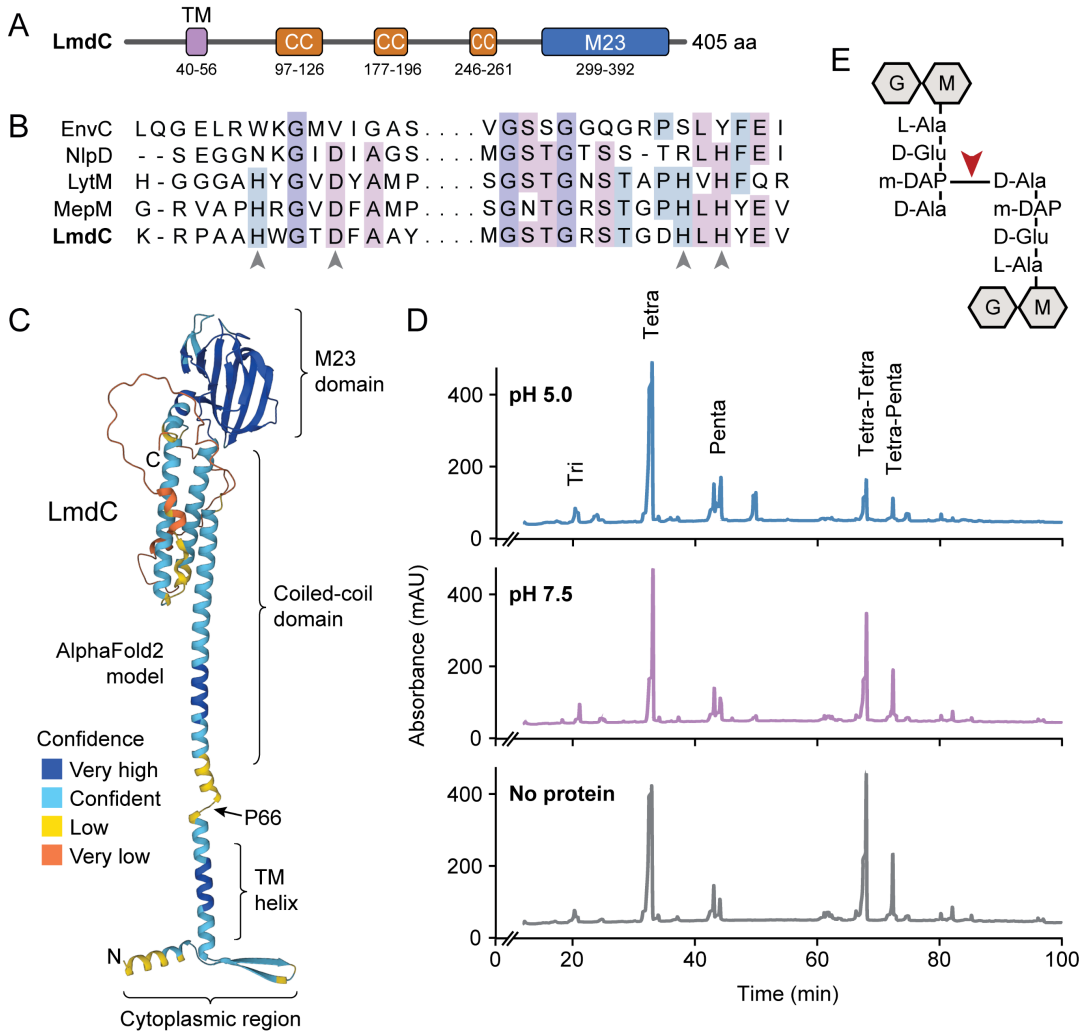

Figure 7. LmdC is a peptidoglycan hydrolase with DD-endopeptidase activity. (A) Predicted domain architecture of *H. neptunium* LmdC. The predicted positions of the transmembrane helix (TM), the three coiled-coil regions (CC) and the M23 peptidase domain are indicated. **(B)** Alignment of the amino acid sequences of multiple M23 peptidases showing the conservation of the catalytic residues in LmdC. Residues required to coordinate the catalytic Zn^{2+} ion of LytM from *S. aureus* (Firczuk et al., 2005) are indicated by arrowheads. The proteins shown are EnvC from *E. coli* (UniProt: P37690), NlpD from *E. coli* (P0ADA3), LytM from *S. aureus* (O33599), MepM from *E. coli* (P0AFS9) and LmdC from *H. neptunium* (Q0BYX6). **(C)** Predicted molecular structure of *H. neptunium* LmdC, generated with Alphafold2 (Jumper et al., 2021). The different domains of the protein and the position of proline 66, which terminates the N-terminal fragment of LmdC used for the *in vivo* analyses in this study ($LmdC_{1-66}$) are indicated. **(D)** HPLC traces showing the muropeptide profile of peptidoglycan treated with LmdC. Cell walls were incubated with the isolated M23 peptidase domain of LmdC at pH 5.0 and pH 7.5. Subsequently, muropeptides were released with cellosyl, reduced and separated by HPLC. A control sample lacked LmdC (No protein). The nature of the major products is indicated above the peaks. Tri, Tetra and Penta stand for N-acetylglucosamine-N-acetylmuramitol tripeptide, tetrapeptide and pentapeptide, respectively. **(E)** Structure of a TetraTetra muropeptide. Abbreviations: G (N-acetylglucosamine), M (N-acetylmuramic acid). The cleavage site of LmdC is indicated by a red arrowhead.

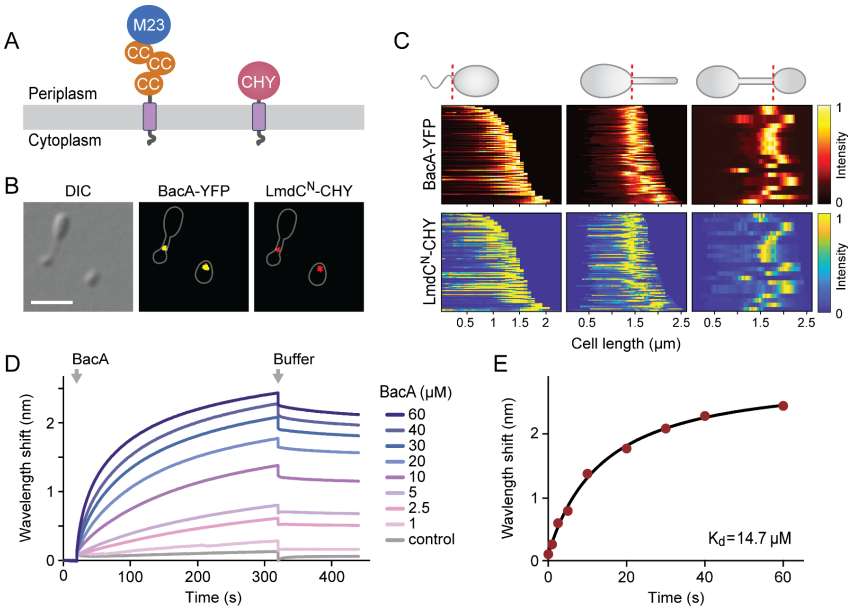

Figure 8. LmdC colocalizes and directly interacts with BacA. (A) Domain architectures of the native LmdC protein and the $LmdC_{1-66}$-mCherry fusion used for co-localization studies. The transmembrane helix is shown in purple. Abbreviations: CC (coiled-coil domain), M23 (M23 peptidase domain), CHY (mCherry). **(B)** Co-localization of BacA-YFP and $LmdC^N$-mCherry in *H. neptunium*. Shown are representative cells of strain MO79 (*bacA*::*bacA-eyfp* P_{Cu}::P_{Cu}-*lmdC*^{N}-*mCherry* that were induced for 2 h with 0.5 mM $CuSO_4$ prior to analysis by DIC and fluorescence microscopy. **(C)** Demographic analysis of BacA-YFP and $LmdC^N$-mCherry co-localization in swimmer (left; n=99), stalked (middle; n=103) and budding (right; n=22) cells from the culture imaged in panel B. Data were analyzed as described for **Figure 4B**. Corresponding fluorescence profiles are shown at the same relative position in the two graphs. **(D)** Bio-layer interferometric analysis of the interaction between cytoplasmic domain of LmdC and BacA. Sensors derivatized with a biotinylated synthetic peptide comprising the N-terminal cytoplasmic region of LmdC (amino acids 1-38) were probed with the indicated concentrations of BacA. After the association of BacA, the sensors were transferred to protein-free buffer to induce BacA dissociation. The interaction kinetics were followed by monitoring the wavelength shifts resulting from changes in the optical thickness of the sensor surface during association or dissociation of the analyte. The extent of non-specific binding of BacA to the sensor surface was negligible (control). **(E)** Affinity of the BacA-LmdC interaction. The maximal wavelength shifts measured in the experiment shown in panel D were plotted against the corresponding BacA concentration. The data were fitted to a one-site binding model, yielding an apparent K_d value of ~15 μM.

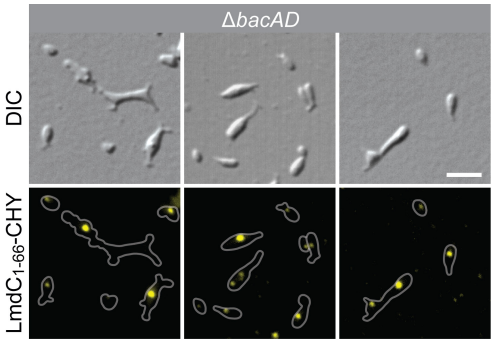

Figure 8—figure supplement 1. Random localization of $LmdC_{1-66}$-mCherry in the Δ*bacAD* background. Cells of strain MO80 (Δ*bacAD* P_{Cu}::P_{Cu}-*lmdC*$_{1-66}$-*mCherry*) were induced for 2 h with 0.5 mM $CuSO_4$ prior to imaging. mCherry fluorescence is shown in yellow. Bar: 3 μm.

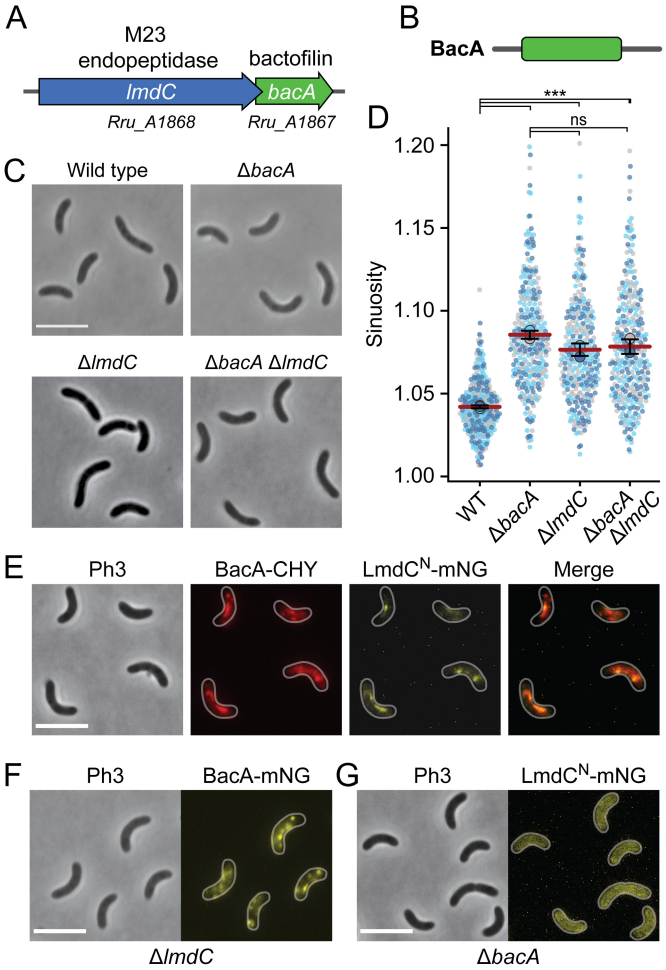

Figure 9. BacA and LmdC contribute to cell morphogenesis in *R. rubrum*. (A) Schematic representation of the *bacA-lmdC* operon in *R. rubrum*. **(B)** Domain organization of BacA from *R. rubrum*. The bactofilin polymerization domain (green box) is flanked by non-structured N- and C-terminal regions. **(C)** Phenotypes of *R. rubrum* wild-type (S1), Δ$bacA_{Rs}$ (SP70), Δ$lmdC_{Rs}$ (SP68) and Δ$bacA_{Rs}$ Δ$lmdC_{Rs}$ (SP116) cells, imaged using phase-contrast microscopy. Bar: 5 µm. **(D)** Superplots showing the distribution of cell sinuosities in populations of the indicated *R. rubrum* strains. Small dots represent the data points, large dots represent the median values of the three independent experiments shown in the graphs (dark blue, light blue, grey). The mean of the three median values is indicated by a horizontal red line. Whiskers represent the standard deviation. *** $p<0.005$; ns, not significant; t-test). **(E)** Co-localization of $BacA_{Rs}$-mCherry and $LmdC^{N}_{Rs}$-mNeonGreen in the Δ$lmdC_{Rs}$ background (SP119). The Pearson's Correlation Coefficient (PCC) of the two fluorescence signals in a random subpopulation of cells (n=87) is 0.515. Scale bar: 5 µm. **(F)** Localization of $BacA_{Rs}$-mNeonGreen in the Δ$lmdC_{Rs}$ background (SP98). Bar: 5 µm. **(G)** Localization of $LmdC_{Rs}$-mNeonGreen in the Δ$bacA_{Rs}$ background (SP118). Bar: 5 µm.

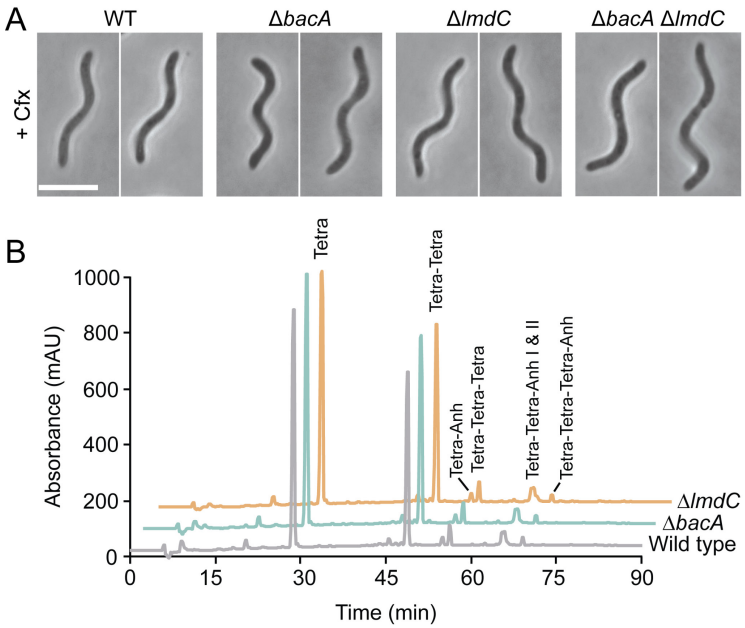

Figure 9—figure supplement 1. Analysis of BacA and LmdC from *R. rubrum*. (A) Clearer visualization of the abnormal curvature of BacA- and LmdC-deficient *R. rubrum* cells by inhibition of cell division. Cells of strains SP68 (Δ*lmdC*), SP70 (Δ*bacA*) and SP116 (Δ*lmdC* Δ*bacA*) were treated with 5 µg/ml cefalexin (Cfx) for 6 h. Bar: 5 µm. **(B)** Muropeptide profiles of different *R. rubrum* strains. Cell walls of strains S1 (wild type), SP70 (Δ$bacA_{Rs}$) and SP68 (Δ*lmdC*) were digested with cellosyl to release muropeptides, which were reduced and separated by HPLC chromatography. The identities of major muropeptide species, assigned based on the previously reported retention times (Glauner, 1988), are given above the corresponding peaks. Tetra stands for N-acetyl-glucosamine-N-acetylmuramitol tetrapeptide. "Anh" indicates muropeptides containing 1,6-anhydromuramic acid.

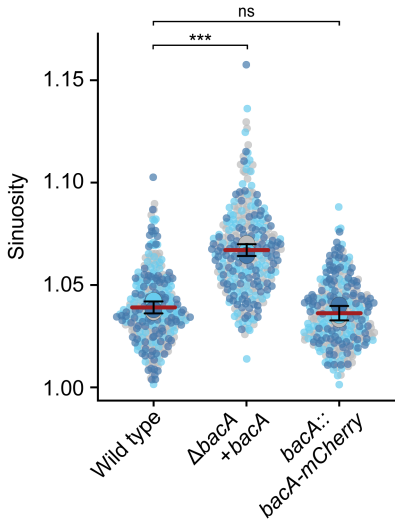

Figure 9—figure supplement 2. Cell lengths of *R. rubrum* strains. Superplots showing the distribution of cell sinuosities in populations of strains S1 (wild type), SP105 (Δ$bacA_{Rs}$ P_{bacA}-$bacA_{Rs}$) and SP109 ($bacA_{Rs}$::$bacA_{Rs}$-*mCherry*). Small dots represent the data points, large dots represent the median values of the three independent experiments shown in the graphs (dark blue, light blue, grey). The mean of the three median values is indicated by a horizontal line. Whiskers represent the standard deviation. *** $p<0.005$; ns, not significant; t-test).

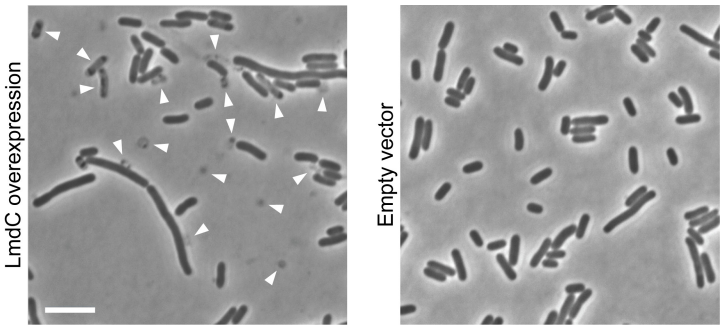

Figure 9—figure supplement 3. Lysis of *E. coli* upon heterologous expression of full-length *R. rubrum lmdC*. Shown are cells of *E. coli* Rosetta(DE3)pLysS harboring pSP120 (P_{T7}-*lmdC*$_{Rs}$) or the corresponding empty vector imaged 4h after the induction of gene expression with 0.5 mM IPTG. Arrowheads indicate ghost cells, cell debris, lysing cells or strongly elongated cells. Scale bar: 5 µm.

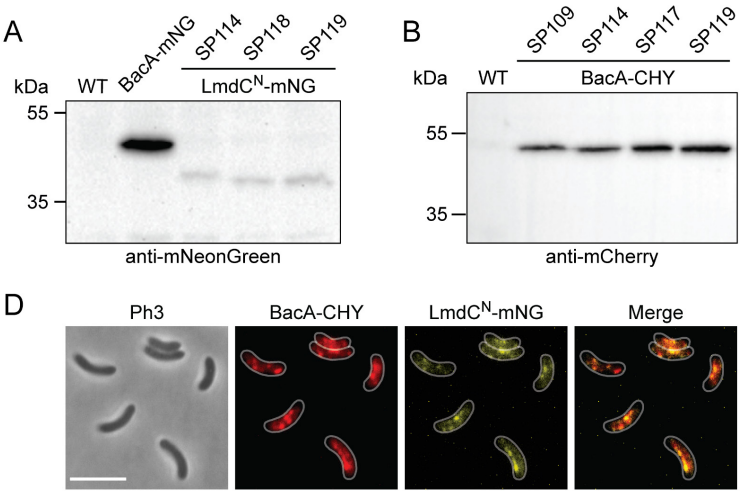

Figure 9—figure supplement 4. Analysis of *R. rubrum* strains producing fluorescent protein fusions. (A) Levels of the LmdC$^N_{Rs}$-mNeonGreen fusion in different *R. rubrum* strains. Strains SP98 (Δ*lmdC*$_{Rs}$ *bacA*$_{Rs}$::*bacA*$_{Rs}$-*mNeongreen*), SP114 (*bacA*$_{Rs}$::*bacA*$_{Rs}$-*mCherry* P_{lmdC}-*lmdC*$^N_{Rs}$-*mNeongreen*), SP118 (Δ*bacA* Δ*lmdC* P_{lmdC}-*lmdC*$_{1-80}$-*mNeongreen*) and SP119 (*bacA*::*bacA-mCherry* Δ*lmdC* P_{lmdC}-*lmdC*$_{1-80}$-*mNeongreen*) were subjected to immunoblot analysis with an anti-mNeonGreen antibody. Predicted molecular weights: BacA$_{Rs}$-mNeonGreen (44.8 kDa), LmdC$^N_{Rs}$-mNeonGreen fusion (35.9 kDa) **(B)** Levels of the BacA$_{Rs}$-mCherry fusion in different *R. rubrum* strains. Strains SP109 (*bacA*$_{Rs}$::*bacA*$_{Rs}$-*mCherry*), SP114 (*bacA*$_{Rs}$::*bacA*$_{Rs}$-*mCherry* P_{lmdC}-*lmdC*$^N_{Rs}$-*mNeongreen*), SP117 (*bacA*$_{Rs}$::*bacA*$_{Rs}$-*mCherry* Δ*lmdC*) and SP119 (*bacA*$_{Rs}$::*bacA*$_{Rs}$-*mCherry* Δ*lmdC* P_{lmdC}-*lmdC*$^N_{Rs}$-*mNeongreen*) were subjected to immunoblot analysis with an anti-mCherry antibody. The predicted molecular weight of BacA$_{Rs}$-mCherry is 44.9 kD. **(C)** Co-localization of BacA$_{Rs}$-mCherry and LmdC$_{Rs}$-mNeongreen in *R. rubrum* cells carrying the native *lmdC*$_{Rs}$ gene. The Pearson's Correlation Coefficient (PCC) of the two fluorescence signals in a random subpopulation of cells (n=177) is 0.54. Scale bar: 5 µm.

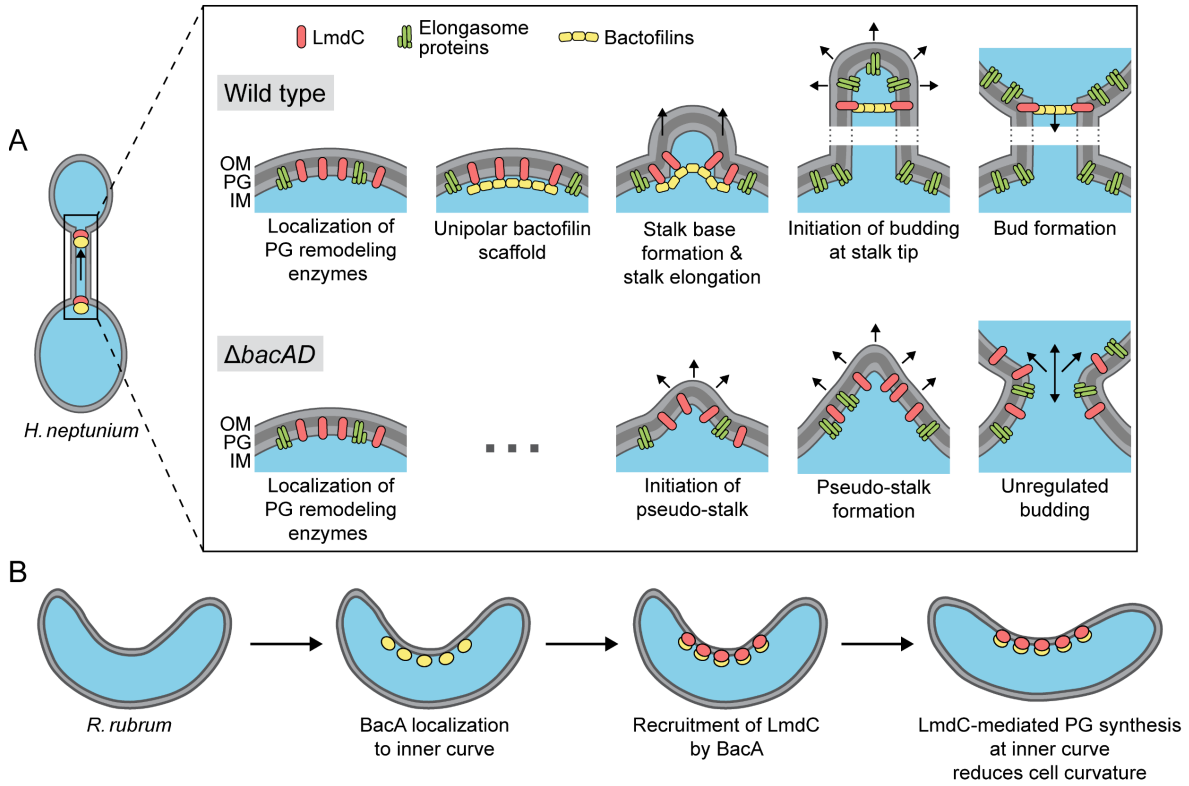

Figure 10. Model of the roles of BacA and LmdC in *H. neptunium* and *R. rubrum* cell morphogenesis. (A) Cell morphogenesis in *H. neptunium* wild-type (top) and Δ*bacAD* cells (bottom). In wild-type cells, BacA polymers form a complex with the DD-endopeptidase LmdC at the future stalked pole. The hydrolytic activity of LmdC helps to curve the cell wall at the incipient stalk base and thus determine stalk morphology. The zone of high positive inner cell curvature, and potentially the physical barrier constituted by the bactofilin polymer, prevent the movement of elongasome complexes from the mother cell body into the stalk, thereby limiting peptidoglycan biosynthesis to the stalked cell pole. At a later stage, the bactofilin-LmdC complex localizes close to the tip of the stalk and again generates a ring-shaped zone of positive cell curvature, thereby promoting the remodeling of the stalk tip into a spherical bud. At the onset of the budding process, elongasome complexes accumulate in the nascent bud by a so-far unknown mechanism. The positively curved bud neck and the bactofilin polymers prevent the movement of elongasome complexes from the bud into the stalk, thereby limiting cell growth to the bud compartment. In the Δ*bacAD* mutant, cells fail to concentrate LmdC at the future stalk base and bud neck. As a consequence, peptidoglycan biosynthesis is no longer limited to the different growth zones, leading to pseudo-stalk formation and unregulated bud expansion. **(B)** Bactofilin-mediated modulation of cell helicity in *R. rubrum*. $BacA_{Rs}$ (yellow) recruits $LmdC_{Rs}$ (red) to the inner cell curvature. The hydrolytic activity of LmdC ultimately stimulates peptidoglycan biosynthesis at this position, leading to a reduction in cell helicity.